

Learning to adapt unknown noise for hyperspectral image denoising

Xiangyu Rui¹, Xiangyong Cao², Jun Shu¹, Qian Zhao¹, Deyu Meng^{1*}

¹School of Mathematics and Statistics and Ministry of Education Key Lab of Intelligent Networks and Network Security, Xi'an Jiaotong University, NO 28 Xianning West Road, Xi'an, 710049, Shaanxi, China.

²School of Computer Science and Technology and Ministry of Education Key Lab For Intelligent Networks and Network Security, Xi'an Jiaotong University, NO 28 Xianning West Road, Xi'an, 710049, Shaanxi, China.

*Corresponding author(s). E-mail(s): dymeng@mail.xjtu.edu.cn;
 Contributing authors: xyrui.aca@gmail.com; caoxiangyong@xjtu.edu.cn;
xjtushujun@gmail.com; timmy.zhaoqian@mail.xjtu.edu.cn;

Abstract

For hyperspectral image (HSI) denoising task, the causes of noise embedded in an HSI are typically complex and uncontrollable. Thus, it remains a challenge for model-based HSI denoising methods to handle complex noise. To enhance the noise-handling capabilities of existing model-based methods, we resort to design a general weighted data fidelity term. The weight in this term is used to assess the noise intensity and thus elementwisely adjust the contribution of the observed noisy HSI in a denoising model. The similar concept of “weighting” has been hinted in several methods. Due to the unknown nature of the noise distribution, the implementation of “weighting” in these works are usually achieved via empirical formula for specific denoising method. In this work, we propose to predict the weight by a hyper-weight network (i.e., HWnet). The HWnet is learned exactly from several model-based HSI denoising methods in a bi-level optimization framework based on the data-driven methodology. For a noisy HSI, the learned HWnet outputs its corresponding weight. Then the weighted data fidelity term implemented with the predicted weight can be explicitly combined with a target model-based HSI denoising method. In this way, our HWnet achieves the goal of enhancing the noise adaptation ability of model-based HSI denoising methods for different noisy HSIs. Extensive experiments verify that the proposed HWnet can effectively help to improve the ability of an HSI denoising model to handle different complex noises. This further implies that our HWnet could transfer the noise knowledge at the model level and we also study the corresponding generalization theory for simple illustration.

Keywords: Hyperspectral image denoising, complex noise, optimization model, learning theory

1 Introduction

Hyperspectral images (HSIs), captured by measuring the electromagnetic spectrum of a scene

across many bands, provide richer information than typical RGB images and can be widely used in many fields, such as remote sensing (Manolakis et al, 2016), agriculture (Lu et al, 2020), food

industry (Liu et al, 2014), and biology (Pyo et al, 2019). However, the collected HSIs are often easily degraded by diverse noise sources including atmosphere, weather, light conditions, calibration errors, sensor sensitivity and many other effects (Chang et al, 2018; Peng et al, 2022a; Li et al, 2023b; Zhuang et al, 2023; Wang, 2019). HSIs corrupted with such uncontrollable and mixed types of noise are undesired and would inevitably affect subsequent HSI applications. Thus HSI denoising is an important pre-processing step to improve the image quality.

HSI denoising task aims to restore the clean HSI $\mathcal{X} \in \mathbb{R}^{h \times w \times b}$ from the observed noisy HSI $\mathcal{Y} \in \mathbb{R}^{h \times w \times b}$. Mathematically, the HSI denoising task can be formulated as the following optimization problem:

$$\hat{\mathcal{X}} = \arg \min_{\mathcal{X}} \ell(\mathcal{Y}, \mathcal{X}) + \lambda R(\mathcal{X}), \quad (1)$$

where $\hat{\mathcal{X}} \in \mathbb{R}^{h \times w \times b}$ is the restored HSI, $\ell(\cdot, \cdot)$ is the loss term that measures the discrepancy between \mathcal{Y} and \mathcal{X} , $R(\cdot)$ is the regularization term to make the problem well-posed, and λ is the trade-off parameter to balance the loss and regularization terms. Based on the model (1), HSI denoising methods can be divided into two categories. One line focuses on exploring the prior knowledge of HSI and design the corresponding $R(\mathcal{X})$. The other line mainly focuses on studying the noise feature and design the loss term $\ell(\mathcal{Y}, \mathcal{X})$. In this work, we follow the latter research line to study the loss term.

To further illustrate how noise information can be embedded into the loss term, we can concretized model (1) into the following weighted form:

$$\hat{\mathcal{X}} = \arg \min_{\mathcal{X}} \underbrace{\frac{1}{2} \|\mathcal{W} \odot (\mathcal{Y} - \mathcal{X})\|_2^2}_{\ell(\mathcal{Y}, \mathcal{X})} + \lambda R(\mathcal{X}). \quad (2)$$

The elements of the weight tensor \mathcal{W} are non-negative. They determine how much each element of \mathcal{Y} can contribute to the problem solution. For example, suppose an area of \mathcal{Y} , e.g., $\mathcal{Y}(\Omega)$, is heavily polluted, and then this area is not “trust-worthy” for construct \mathcal{X} . Thus, it is reasonable to assign a small weight to $\mathcal{Y}(\Omega)$ in model (2) such that $(\mathcal{Y} - \mathcal{X})(\Omega)$ is not supposed to be too small,

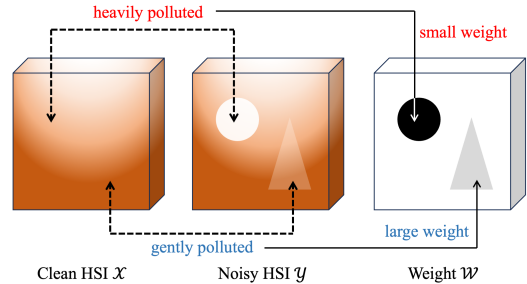


Fig. 1: The circular area is more heavily polluted, and then smaller weights should be assigned. Comparatively, the triangular area is more gently polluted, and then relatively larger weights should be assigned.

which is also consistent with the actual circumstances. A toy example is shown in Fig. 1. From this, we can observe that a reasonable \mathcal{W} and noise information are deeply correlated. However, determining the value of \mathcal{W} according to noise is rather challenging because the noise embedded in an HSI is usually too complex to characterize. In previous HSI denoising works, one shortcut approach is to set all the values of \mathcal{W} to one. In this way, $\ell(\mathcal{Y}, \mathcal{X})$ does not take into consideration the variability of noise distribution within an HSI, which would inevitably limit the model performance.

Existing methods for computing a non-trivial \mathcal{W} mainly take the following forms. a) \mathcal{W} is set by an empirical formula which follows the rule that \mathcal{W} should be inversely proportional to the estimated noise intensity (He et al, 2015a). b) \mathcal{W} is a binary tensor taking values 0 or 1. Specifically, 0 means the noise in this position is classified as sparse noise and 1 as Gaussian noise (Zhuang and Ng, 2021). Thus, the areas that contains “sparse noise” do not contribute to the reconstruction. c) From the perspective of statistics, \mathcal{W} is considered to be related to a hypothetical noise distribution and is updated via inference algorithms such as Expectation-Maximization (EM) (Meng and De La Torre, 2013; Cao et al, 2016; Chen et al, 2017a; Yue et al, 2018; Jiang et al, 2021). We see that the above methods have made tremendous efforts to extract the noise information and condense it into the single weight tensor \mathcal{W} . Subsequently, a question is raised that if it is possible for \mathcal{W} to break free from the constraints of either empirical formulation or hypothetical noise distribution, while \mathcal{W} is able to be automatically and

properly pre-specified based on the characteristics of data and model.

To address the issue, in this work, we propose a novel strategy to predict the weight \mathcal{W} in the loss term $\frac{1}{2}\|\mathcal{W} \odot (\mathcal{Y} - \mathcal{X})\|_2^2$. Specifically, the weight \mathcal{W} is predicted automatically by a parameterized “weight function”, and in this work, we use a neural network h_θ (called hyper-weight network or HWnet). The HWnet takes the noisy HSI, which contains all noise information, as input and directly generates the weight as output. Unlike previous works that design the weight function empirically or hypothetically, we consider leaving the denoising models in the form (2) themselves to determine this weight function. There are two basic but very important facts to help to realize such idea. One is that different weights would produce different solutions in one model (2) and thus the best solution should imply the most suitable weight. The other is that different models (i.e. with different $R(\mathcal{X})$) would also produce different restored HSIs. Against such issues, in this study we describe the implicit relationship between the restored HSI and its proper weight function by a bilevel optimization framework given noisy/clean HSI training pairs. Specifically, such a bilevel framework is composed of two sub-problems. The lower-level subproblem leverages multiple denoising models of form (2) to generate the restored HSIs by optimizing these models. Each of them contains the same weight predicted by an explicit weighting function h_θ mapping from an HSI to its imposed weight setting. The upper-level subproblem aims to optimize the parameters θ of h_θ by minimizing the discrepancy between the restored and corresponding ground-truth HSIs. The above bi-level optimization process finishes the training of h_θ . We see that h_θ is essentially guided to learn to extract the noise information from models and training pairs with very specific physical meaning. Then, h_θ can be readily used to estimate the weight of other unseen noisy HSIs. Subsequently, the predicted weight helps to enhance the performance of a denoising model (2) to adapt to complex noise.

Furthermore, a trained h_θ is also ready to be used for a new denoising model (namely, target models) with different regularizer terms from training by implementing the weight predicted by h_θ . This is a key property of h_θ considering the fact that denoising models with remarkable

performance always have complicated formulations that may not be able to train h_θ . However, we can choose several simpler denoising models (namely, source models) for training. This would raise another question. What effect does the choice of the source models have on the performance of the target model? To analyze such generalization ability of h_θ at the level of model, we have conducted several experiments and observe their results. Besides, we have also preliminarily established a theoretical analysis about the generalization error from the source models to the target model by the proposed task divergence, which should help us to understand the generalization behavior of h_θ across HSI denoising models.

In summary, the contribution of this study is as follows:

1. We propose a new strategy to predict the weight of the loss term in an HSI denoising model. Specifically, the weight is predicted through a neural network h_θ , namely HWnet. Different from existing methods that require empirical weight formulation or hypothetical noise distribution, our h_θ is trained in a data-driven manner that learns the noise information directly from the denoising models themselves.
2. The learned h_θ can directly predict weights for new noisy HSIs and the weight can help to improve the complex noise removal performance of the denoising model. Extensive experiments demonstrate the capability of our HWnet to handle various complex noises.
3. The learned h_θ is ready to be used for a new HSI denoising model with different regularizer terms. Substantial experiments about the source model combinations and their effects on different target models show that h_θ has good generalization ability at the model level.
4. Some preliminary theories are established to analyze the generalization error of HWnet at the model level. The theories help to understand how the choice of source models would have on the target model.

The rest of this work is organized as follows. Sec. 2 reviews existing HSI denoising models and presents relevant learning theory works. Sec. 3 presents our method to predict the weight and discussions about the weight. Additionally, the

theoretical analysis of generalization error of our method is provided. Sec. 4 demonstrates experiments to verify the generalization ability of our HWnet both on different noise patterns and different models from training ones. The paper is then concluded.

This work is the extension of our previous work (Rui et al, 2021). In (Rui et al, 2021), we have made an early but relatively rough attempt on the weighting strategy. In this study, we completely eliminate the require of any prior knowledge of the weight or noise and instead allow the denoising models to fully determine the weight function. Consequently, we have made new comprehensions of our weight function from the model level, conducted more sufficient experiments, and built relevant learning theories to analyze the proposed method. More extension details have been stated in Online Resource 2.

2 Related Works

In this section, we will briefly review the existing HSI denoising methods and some related learning theory research.

2.1 HSI Denoising Methods

Existing HSI denoising methods can be roughly divided into two categories, i.e. model-based approaches and deep-learning-based ones. In the following, we will introduce the two types of methods separately.

2.1.1 Model-based HSI Denoising Approaches

The model-based HSI denoising methods aim to restore the clean HSI by fully investigating the image priors. One of the most important HSI prior is the low-rank property, mainly characterizing the evident correlation along the spectral dimension of general HSIs. One typical method is LRMR (Zhang et al, 2013), which formulates HSI denoising as a robust nuclear norm minimization (NNM) model. Subsequently, (He et al, 2015a) proposed to spatially split the HSI into patches and then solve the NNM problem with noise level adjustment. Beyond the convex nuclear norm regularizer, (Chen et al, 2017b) further proposed a non-convex regularizer to induce sparsity.

Regarding the HSI as a three-dimensional tensor, low-rank tensor decomposition approaches have also attracted much attention. Typically, (Xue et al, 2019) used CANDECOMP/PARAFAC decomposition and the average nuclear norm along each mode to describe the low-rank property. (Xie et al, 2017) considered Tucker decomposition and the sparsity on the core tensor. (Chen et al, 2019) applied tensor-ring decomposition to better preserve the HSI intrinsic property. (Lin et al, 2020) used t-SVD to describe tensor low-tubal rankness. Another widely used HSI prior is the total variation (TV), which encodes the smoothness prior of HSIs along both spectral and spatial dimensions (Yuan et al, 2012; Aggarwal and Majumdar, 2016; Peng et al, 2020; He et al, 2015b; Wang et al, 2017; Jiang et al, 2016). For example, (Yuan et al, 2012) used the weighted Frobenius norm on the gradient map as regularization. (Aggarwal and Majumdar, 2016) applied spectral difference operator on spatial gradient map to additionally describe the HSI spectral correlation. (Peng et al, 2020) proposed an enhanced TV regularization by calculating sparsity on subspace bases of gradient maps along all bands of an HSI. Sparse representation is also a commonly used prior to capture the sparsity of representative coefficients under some bases. Typically, (Lu et al, 2015) considered measuring the spatial and spectral correlation of an HSI and then used the correlation to split the HSI into patches before performing sparse representation. (Wei et al, 2017) applied modified structured sparse coding to capture the underlying HSI prior. Additionally, more recent researches consider several HSI priors simultaneously. Along this line, (He et al, 2015b) jointly utilized the low-rank property in the spectral dimension and the total variation constraint in the spatial dimension. (Zhao and Yang, 2014) applied both sparse representation and low-rank constraint to formulate the denoising model. Other prior properties of HSI have also been attempted. E.g., (Chang et al, 2017) took mode-2 unfolding of an HSI with more low rankness than the other two modes. (He et al, 2020) performed low-rank matrix decomposition along the spectral mode and used WNNM (Gu et al, 2017) to denoise the reduced image. (Zheng et al, 2020) placed group sparsity on the gradient maps of the reduced image and also set the continuity constraint on the spectral factor matrix.

In addition to exploiting HSI priors, designing a proper loss term to describe the noise property is also an alternative. Typical methods assume HSI mainly contains two types of noise, i.e., Gaussian noise and sparse noise, and adopt ℓ_2 and ℓ_1 losses to tackle the noise separately. Specifically, (He et al, 2015a) pre-estimated the noise variance of each band and then proposed a vague weighted ℓ_2 model whose weights are directly related to noise variance by a fixed empirical mapping. (Ma et al, 2016) utilized a $\ell_{2,1}$ -norm loss to robustly handle noise and outliers. (Zheng et al, 2020) applied the weighted ℓ_1 loss term where the weight is proportional to the sparse residual for each iteration (Candes et al, 2008). Another series of methods is called noise modeling (Meng and De La Torre, 2013; Cao et al, 2016; Chen et al, 2017a; Yue et al, 2018), which firstly assumes the HSI noise follows a broad class of distribution and then constructs the loss function based on the maximum likelihood estimation (MLE) or variational inference (VI) principle. For example, (Meng and De La Torre, 2013) assumed the additive noise obeys the mixture of Gaussian (MoG) distribution which theoretically can approximate any continuous distribution. Later, (Cao et al, 2016) established a mixture of exponential power (MoEP) distribution to model the noise. Further, (Chen et al, 2017a) claimed that the noise in a natural HSI is always with a more complicated non-independent and identically distributed (non-i.i.d) structure. (Yue et al, 2018) hypothesized that the noise of HSI in each band is depicted by a Dirichlet process Gaussian mixture model (DP-GMM). Similarly, (Jiang et al, 2021) applied the mixture of Gaussian (MoG) distribution to model noise and the corresponding M-step corresponds to a weighted ℓ_2 model. (Zhuang and Ng, 2021) classified the noise patterns using MoG and only used the Gaussian-noise-whitened components to restore the HSI. In summary, most of the above HSI denoising models are essentially weighted-loss models, where the weight is specified subjectively or empirically. In this work, instead of pre-defining the weight update equation empirically or pre-assuming the noise distribution subjectively, we design a novel approach to make this weight setting aim able to be automatically implemented.

2.1.2 Deep-Learning-based HSI Denoising Approaches

Recently, deep learning (DL) methods have been extensively studied in the HSI denoising problem, where denoising is implemented by learning an explicit nonlinear mapping from noisy/clean HSI pairs. (Chang et al, 2018) is the first work to adopt a convolutional neural network (CNN) for HSI denoising, where 2D convolution and dilation convolution are used. Later, (Yuan et al, 2018) fused the adjacent bands of HSI to utilize both the spatial and spectral features in the deep residual CNN. (Shi et al, 2021) further applied 3D convolution instead of 2D convolution together with self-attention to extract HSI features. (Wei et al, 2020) also adopted 3D convolution, quasi-recurrent pooling function, and alternating directional structure to design the network. Besides, (Lin et al, 2019) combined the matrix factorization method with CNN, where the CNN is used as a solver of the corresponding sub-problem. (Cao et al, 2021) used two reasoning modules to carefully extract both global and local spatial-spectral features. (Pang et al, 2022) designed a new HSI denoising network by combining the CNN and transformer. Further, to tackle the physical interpretability issue of the deep neural network (DNN), (Xiong et al, 2020; Bodrito et al, 2021) proposed a model-guided spectral-spatial network by unfolding the iterative algorithm to solve the sparse model. Afterwards, (Xiong et al, 2021) introduced an end-to-end model-aided non-local neural network to simultaneously consider the spectral low-rank model and spatial deep prior. (Zhang et al, 2021)(Zhang et al, 2022) propose a new real Hyperspectral image dataset. (Li et al, 2023a) and (Li et al, 2023b) introduce transformer structures to extract the spatial and spectral features of HSIs. Although the aforementioned DL-based HSI denoising methods have achieved excellent performance in many applications, their performance largely relies on complex network architecture design and the quality and quantity of training data and often lacks good generalization capability.

2.2 Learning Theory on Generalization

The learning theory serves as the cornerstone for the machine learning fields and has been closely concerned for decades. It has gained great development in transfer learning (Dai Wenyuan et al, 2007)(Mahmud and Ray, 2007), domain adaption (Ben-David et al, 2010)(Cortes and Mohri, 2011)(Germain et al, 2016)(McNamara and Balcan, 2017), domain generalization (Blanchard et al, 2011)(Muandet et al, 2013)(Blanchard et al, 2021)(Sicilia et al, 2021), and so on. For example, (Maurer et al, 2016)(Tripuraneni et al, 2020) considered the generalization theory of the method that learns the common representation from several training tasks and generalizes to new tasks from the perspective of task diversity. (Shu et al, 2021) studied the generalization theory of the approach that learns a universal hyper-parameter prediction policy for a group of tasks. The generalization theories of these works are developed mainly based on a pre-assumed common environment in which all tasks are drawn. Additionally, the diversity of the environment should be bounded by the diversity of training tasks so that the generalization makes sense.

In this study, inspired by these related generalization researches, we prove the generalization theory of our proposed weight prediction scheme for the HSI denoising model. The main differences between our method and other generalization theories are as follows. Firstly, we turn to measure the individual task divergence rather than the abstract environment, which is more pertinent to our problem. Secondly, the existing generalization theory works mainly focus on high-level classification problems, while our work should be the first generalization theory work in the field of low-level vision to the best of our knowledge.

3 Proposed Method

As mentioned in the introduction section, we want to break free from the empirical formulation or hypothetical noise distribution when designing weight. Thus, a parameterized function is utilized to build a mapping from the noisy HSI \mathcal{Y} to its weight \mathcal{W} which is supposed to reflect noise

information:

$$\mathcal{W} = h_{\theta}(\mathcal{Y}), \quad (3)$$

where $h_{\theta}(\cdot)$ is a hyper-weight network (i.e., HWnet) with parameter θ . The HWnet h_{θ} receives the noisy HSI \mathcal{Y} as the input and generates the weight \mathcal{W} as the output. Correspondingly, the loss term $\frac{1}{2}\|\mathcal{W} \odot (\mathcal{Y} - \mathcal{X})\|_F^2$ can be rewritten as $\frac{1}{2}\|h_{\theta}(\mathcal{Y}) \odot (\mathcal{Y} - \mathcal{X})\|_F^2$. In this section, we will introduce our method about the weight function h_{θ} for HSI denoising model, including its training and practical application, which is shown in Fig. 2. Besides, we also visualize the weights predicted by our HWnet h_{θ} to present their physical meaning. Table 1 presents necessary notations that are used in this study.

3.1 Training HWnet h_{θ} using multiple source models

Combining Eq. (3), we can rewrite problem (2) as

$$\hat{\mathcal{X}}(\mathcal{Y}, \theta, R) = \arg \min_{\mathcal{X}} \frac{1}{2}\|h_{\theta}(\mathcal{Y}) \odot (\mathcal{Y} - \mathcal{X})\|_2^2 + \lambda R(\mathcal{X}). \quad (4)$$

Here, the solution to the optimization problem (2), i.e., the restored HSI $\hat{\mathcal{X}}$, has a mapping relation with three elements. Without a doubt, the noisy HSI \mathcal{Y} is the basic element to find $\hat{\mathcal{X}}$. The second element is the network parameter θ . It first determines the weight $\mathcal{W} = h_{\theta}(\mathcal{Y})$ and then the weight influences the optimization results. The third element is the regularization term R which distinguishes the denoising models. Different denoising models would also result in different restored HSIs. Overall, the noisy HSI \mathcal{Y} , the network parameter θ and the model regularization R determine the final restored HSI $\hat{\mathcal{X}}$. Fig. 3 briefly shows their relationship. Note that such mapping relation is implicit because it is achieved by solving an optimization problem.

From Eq. (4), it is clear that to train network θ , we need “clean/noisy” training data and denoising models. Thus, a bi-level optimization framework is formulated as follows:

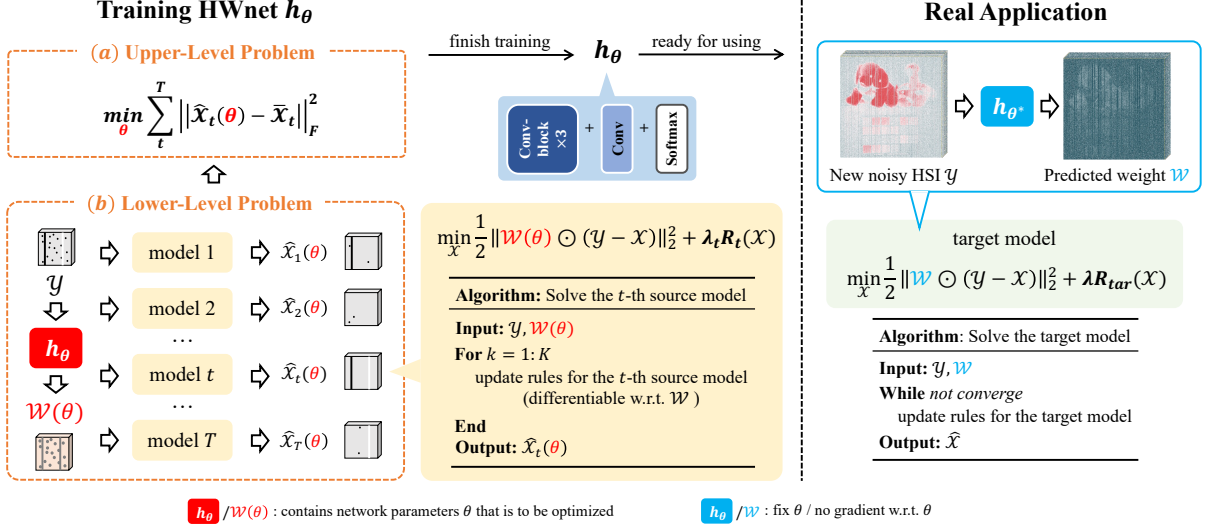


Fig. 2: Overview of the proposed method. The left part shows the training process of the proposed weight function h_θ . This process contains a lower-level problem that solves T HSI denoising problems which are implemented with h_θ , and an upper-level problem that minimizes the distance between the restored image $\hat{\mathcal{X}}(\theta)$ and the ground-truth image $\bar{\mathcal{X}}$. The right part shows the application of HWet h_θ . In this stage, a trained h_θ predicts the weight of a noisy HSI for a target HSI denoising model to help the model better handling complex noise and achieve better performance.

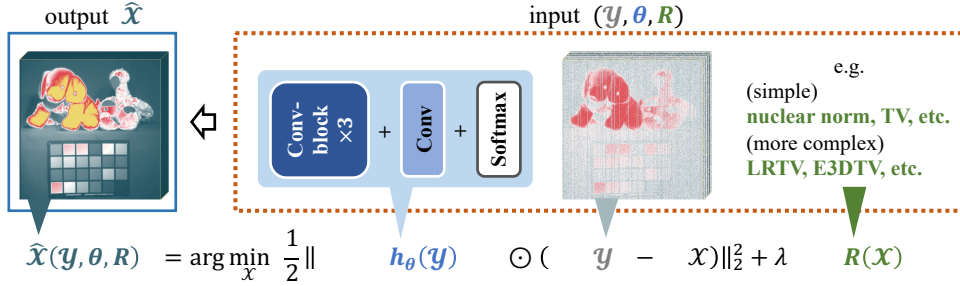


Fig. 3: The solution $\hat{\mathcal{X}}$ to a denoising problem is related three elements. They are the noisy HSI \mathcal{Y} , the network parameter θ (because $\mathcal{W} = h_\theta(\mathcal{Y})$) and the regularization term $R(\mathcal{X})$.

$$\begin{cases} \min_{\theta} \frac{1}{T} \sum_{t=1}^T \frac{1}{N_t} \sum_{i_t=1}^{N_t} \|\hat{\mathcal{X}}_{ti_t}(\theta) - \bar{\mathcal{X}}_{ti_t}\|_2^2, & (5a) \\ \hat{\mathcal{X}}_{ti_t}(\theta) = \arg \min_{\mathcal{X}} \\ \frac{1}{2} \|h_\theta(\mathcal{Y}_{ti_t}) \odot (\mathcal{Y}_{ti_t} - \mathcal{X})\|_2^2 + \lambda_t R_t(\mathcal{X}), t \in [T]. & (5b) \end{cases}$$

Problem (5a) and (5b) are called upper-level and lower-level problems, respectively. There are T different denoising models in the lower-level problem

(5b). $R_t(\mathcal{X})$ is the regularization term of the t -th denoising model. The training dataset is written as $\{(\mathcal{Y}_{ti_t}, \bar{\mathcal{X}}_{ti_t})\}_{i_t=1}^{N_t} \}_{t=1}^T$, where \mathcal{Y}_{ti_t} means the i_t -th noisy HSI for the t -th denoising model and $\bar{\mathcal{X}}_{ti_t}$ is the corresponding ground-truth HSI. N_t is the number of training pairs for the t -th model. For convenience, $\hat{\mathcal{X}}_{ti_t}(\theta)$ is the abbreviation for $\hat{\mathcal{X}}(\mathcal{Y}_{ti_t}, \theta, R_t)$, which means the solution to the t -th denoising model with noisy HSI \mathcal{Y}_{ti_t} .

It should be indicated that training h_θ using the proposed bi-level optimization framework (5a)-(5b) does not rely on extra knowledge about

Table 1: Necessary notations in this work.

$a * b$	the multiplication between a and b
$a \times b$	the size of a matrix
A/B	element-wise division
A^2	element-wise square
$A \geq (\leq) B$	element-wise comparison
\odot	element-wise multiplication
$\ \cdot\ _2$	Frobenius norm for matrices and tensors, or l_2 norm for vectors
$\langle \cdot, \cdot \rangle$	inner product
$\mathcal{N}(0, 1)$	standard Gaussian distribution
\mathbb{E}	expectation
$[N]$	$\{1, 2, \dots, N\}$

weight \mathcal{W} . It completely allows the denoising models to decide the weight function h_θ because the output of h_θ serves the same role as the general weights in the denoising model. Besides, the lower-level problem (5b) produces the restored HSI from different denoising models using the same weight function h_θ . Thus, h_θ is able to integrate noise information provided by multiple models. This should be important because h_θ trained by a single denoising model would inevitably be more advantageous for that model. Then, in the upper-level problem (5a), the network parameter θ is optimized by minimizing the distance between $\hat{\mathcal{X}}$ and $\bar{\mathcal{X}}$, the former of which carries the “weighting rule” from h_θ .

To solve this bi-level optimization problem, we utilize a simple yet efficient way. The denoising models in the lower-level problem can usually be solved by applying appropriate algorithms. For example, in Algorithm 1, we show the general form of applying Alternating Direction Method of Multipliers (ADMM) (Boyd et al, 2011). Details of how to get Algorithm 1 are included in Appendix A. Besides, there are two points to concern for the lower-level problem. First, when training h_θ , we need to set an appropriate number of steps to run the algorithm because it usually takes many steps for the algorithm to converge while the computational graph of each step has to be stored. Second, each updating rule in the algorithm should be differentiable with respect to (w.r.t.) their variables such that the final $\hat{\mathcal{X}}$ is differentiable w.r.t. \mathcal{W} . Thus, we tend to choose simple denoising models (source models) when

Algorithm 1 An example of ADMM algorithm to solve denoising problem (2)

Input: noisy HSI \mathcal{Y} , weight \mathcal{W} , trade-off parameter λ .

Initialization: $\mathcal{X}, \mathcal{Z}, \Gamma, \mu$

- 1: **while** not convergence **do**
 - 2: $\mathcal{Z} \leftarrow \frac{\mathcal{W}^2 \odot \mathcal{Y} + \mu \mathcal{X} + \Gamma}{\mathcal{W}^2 + \mu}$
 - 3: $\mathcal{X} \leftarrow \arg \min_{\mathcal{X}} \frac{\mu}{2} \left\| \mathcal{X} - \left(\mathcal{Z} - \frac{\Gamma}{\mu} \right) \right\|_2^2 + \lambda R(\mathcal{X})$
 - 4: $\Gamma \leftarrow \Gamma + \mu(\mathcal{X} - \mathcal{Z})$
 - 5: **end while**
 - 6: **Output:** $\hat{\mathcal{X}} = \mathcal{X}$
-

designing the lower-level problem for more efficient training. For example, denoising models with nuclear norm or total variation norm as regularization usually have closed-form solutions for the corresponding \mathcal{X} -subproblem (update \mathcal{X}) and are relatively easy to optimize. Now suppose that the derivative $\partial \hat{\mathcal{X}} / \partial h_\theta$ (i.e., $\partial \hat{\mathcal{X}} / \partial \mathcal{W}$) exists and is tractable, by chain rule, the gradient used to update the network parameter θ can be represented by

$$\nabla \theta = \frac{1}{T} \sum_{t=1}^T \frac{1}{N_t} \sum_{i_t=1}^{N_t} \frac{\partial \left\| \hat{\mathcal{X}}_{ti_t}(\theta) - \bar{\mathcal{X}}_{ti_t} \right\|_2^2}{\partial \hat{\mathcal{X}}_{ti_t}(\theta)} \frac{\partial \hat{\mathcal{X}}_{ti_t}(\theta)}{\partial h_\theta} \frac{\partial h_\theta}{\partial \theta} \quad (6)$$

In Algorithm 2, we summarize the entire training process of our HWnet h_θ .

In this work, the HWnet h_θ is designed as a simple four-layer convolutional neural network (CNN). Similar to (Rui et al, 2021), the first three layers of h_θ borrow the “pseudo-3D” convolution structure (Qiu et al, 2017), which takes the form of “ $3 \times 3 \times 1$ conv + ReLU + $1 \times 1 \times 3$ conv”. Each layer is followed by the “ReLU” activation function. Batch normalization is not used since it inclines to decrease the noise distinction between data. The final layer takes the full “ $3 \times 3 \times 3$ ” convolution. The output of the final convolutional layer is activated by the softmax function and then multiplies $h * w * b$. Thus the predicted \mathcal{W} is averaged to 1.

Algorithm 2 Solve the bi-level problem (5a)-(5b)

Require: training dataset $\{(\mathcal{Y}_{t_i}, \bar{\mathcal{X}}_{t_i})\}_{i=1}^{N_t}$, T denoising models.
1: **while** not converge **do**
2: **for** $t = 1 : T$ **do**
3: **for** $i_t = 1 : N_t$ **do**
4: predict weight $\mathcal{W}_{t_i} = h_\theta(\mathcal{Y}_{t_i})$
5: $\hat{\mathcal{X}}_{t_i}(\theta) = \arg \min_{\mathcal{X}} \frac{1}{2} \|\mathcal{W}_{t_i} \odot (\mathcal{Y}_{t_i} - \mathcal{X})\|_2^2 + \lambda_t R_t(\mathcal{X})$
6: **end for**
7: **end for**
8: calculate gradient $\nabla \theta$ by Eq. (6)
9: update θ
10: **end while**
11: **Output:** h_θ

3.2 Applications of HWnet h_θ

3.2.1 General framework

Learning a weight function is not the final destination for HSI denoising. In the training phase, h_θ learns how to extract noise information from a noisy HSI and generate the corresponding weight. The weight should be used for a determinate HSI denoising model to better remove complex noise. The implementation of a trained h_θ is straightforward. Specifically, the loss term $\|h_\theta(\mathcal{Y}) \odot (\mathcal{Y} - \mathcal{X})\|_2^2$ is plugged into a target HSI denoising model. The consequent general form of application of h_θ is as follows:

$$\min_{\mathcal{X}} \frac{1}{2} \|\mathcal{W} \odot (\mathcal{Y} - \mathcal{X})\|_2^2 + \tau R_{tar}(\mathcal{X}),$$

where $\mathcal{W} = h_\theta(\mathcal{Y})$. (7)

Note that the target model does not necessarily have to belong to the source models. If the goal is to achieve better performance, denoising models usually need to be carefully designed and the regularizations are complex. However, training convenience and efficiency are the main principles of selecting source models. The denoising problem (7) is solved as general optimization problems using some common algorithms including proximal gradient (PG) (Shi et al, 2015), half quadratic splitting (HQS) (Sun et al, 2020) and ADMM (Boyd et al, 2011) which has been introduced in Algorithm 1.

There are also some special cases of problem (7). For example, when the deep image prior (DIP) (Ulyanov et al, 2018; Lehtinen et al, 2018; Luo et al, 2021) is implemented as image regularization, problem (7) can be modified into the following form:

$$\min_{\eta} \|\mathcal{W} \odot (g_\eta(\mathcal{Z}) - \mathcal{Y})\|_2^2 + \tau R(g_\eta(\mathcal{Z})),$$

where $\mathcal{W} = h_\theta(\mathcal{Y})$. (8)

In problem (8), $g_\eta(\cdot)$ is a deep neural network (DNN) that takes random noise \mathcal{Z} as input and generates the denoised image as output. Difference between general model (7) and DIP model (8) lies on that the structure of $g_\eta(\cdot)$ also provides implicit image regularization. Once the training is finished, i.e., the optimal parameter η^* is learned, the restored image $\hat{\mathcal{X}}$ can be immediately obtained as $g_{\eta^*}(\mathcal{Z})$.

Compared with previous methods, our h_θ can directly generate the proper weight and the underlying weighting rules are learned from data and models. Besides, our h_θ is not designed for one specific model. It can be easily implemented to different models with different regularization terms while bringing almost no increase in algorithm complexity.

3.2.2 Theoretical analysis

When the source model is the same as the target model, we get the ideal h_θ for the target model. On the contrary, there exists “error” when we apply h_θ if the source and the target models are different. Specifically, such “error” can be described as the difference between the average performance of the utilized h_θ and the ideal h_θ implementing on the target model. We use “ \mathbf{E}_g ” to refer to the error, which is also called the generalization error. In this section, we will present a preliminary estimation of the upper bound related to the generalization error.

More generally speaking, suppose there are S target models of the form in problem (2). They are written as

$$\min_{\mathcal{X}} \frac{1}{2} \|\mathcal{W} \odot (\mathcal{Y} - \mathcal{X})\|_2^2 + \lambda_t R_t(\mathcal{X}),$$

($t = T + 1, \dots, T + S$), (9)

For convenience, the subscript character used in (5b) for T source models continues to be used for the S target models, while the index for target models start counting from $T+1$ and ends at $T+S$. Then our main result about the error \mathbf{E}_g brought by transferring a learned h_θ to target models is presented in the following theorem.

Theorem 1 (Generalization error). *Suppose that Assumptions 1, 2 and 3 hold, $\{R_t\}_{t=0}^T$ are convex and closed, solution to the denoising problem (2) is approximated by the form of $\mathbf{I} - \frac{\lambda}{h^2} \odot \nabla R$. Then for any $\delta > 0$, with probability at least $1 - \delta$, we have*

$$\begin{aligned} \mathbf{E}_g \leq & 6L_n \bar{L}_H \hat{\mathbf{G}}_S(\mathcal{H}) + \frac{6B_l}{T} \sqrt{\sum_{t=1}^T \frac{1}{N_t}} \sqrt{\frac{\log \frac{2}{\delta}}{2}} \\ & + \mathbb{E}_{(\mathcal{Y}, \mathcal{X}) \sim \mathcal{D}} \left\{ \frac{8B_d}{\sqrt{M}\varepsilon} A_1 \right\} + \mathbb{E}_{(\mathcal{Y}, \mathcal{X}) \sim \mathcal{D}} \left\{ \frac{2}{M\varepsilon^2} A_2 \right\}, \end{aligned} \quad (10)$$

where

$$\begin{aligned} A_1 &= \left\| \left(\frac{1}{T} \sum_{t=1}^T \lambda_t \nabla R_t - \frac{1}{S} \sum_{t=T+1}^{T+S} \lambda_t \nabla R_t \right) (\mathcal{Y}) \right\|_2, \\ A_2 &= \left| \frac{1}{T} \sum_{t=1}^T \left\| (\lambda_t \nabla R_t) (\mathcal{Y}) \right\|_2^2 - \frac{1}{S} \sum_{t=T+1}^{T+S} \left\| (\lambda_t \nabla R_t) (\mathcal{Y}) \right\|_2^2 \right|. \end{aligned}$$

In the above theorem, “D” means the data joint distribution, \mathcal{H} is the hypothesis set that contains all possible h_θ captured by θ , and “ $L_n, \bar{L}_H, B_l, B_d, M, \varepsilon$ ” are constants (see Appendix B for details). Theorem 1 mainly says that the generalization error \mathbf{E}_g can be upper bounded by four terms. The first two terms, i.e., $6L_n \bar{L}_H \hat{\mathbf{G}}_S(\mathcal{H})$ and $6B_l/T \sqrt{\sum_{t=1}^T 1/N_t} \sqrt{\log(2/\delta)/2}$ are about the training error, which is caused by the finite quantity of training data. Specifically, the first term describes the complexity of the space of h_θ . The second term is mainly about the training data size and δ . Here, we do not make further explanation for the first two terms because they are irrelevant to the denoising models (please see Appendix B.2 for more discussions).

Our main interest lies on the last two terms, i.e., $\mathbb{E}_{(\mathcal{Y}, \mathcal{X}) \sim \mathcal{D}} \{8B_d/\sqrt{M}/\varepsilon A_1\}$ and $\mathbb{E}_{(\mathcal{Y}, \mathcal{X}) \sim \mathcal{D}} \{2/M/\varepsilon^2 A_2\}$. They both contain the regularization gradient¹ and each of them reveals one kind of “model divergence” between source and target models. Specifically, A_1 directly calculates the difference function between the averaged source regularization gradients and the averaged target regularization gradients. A_2 first calculates the norm value of each regularization gradient on noisy HSI \mathcal{Y} , and then calculates the difference between averaged source norm values and averaged target norm values. We think that A_1 mainly cares about the total regularizations contained in the source and target models respectively, while A_2 distinguishes those regularizations included in each model in more detail. A special case is when the target and source models are the same, then the last two terms reach their minimum value, i.e., zero, which trivially means that there is no error brought by the models. More details are presented in Appendix B.3.

In Sec. 4.5.1, we show some connections between Theorem 1 and simple experiments. But it is also faithful to say that the real applications are much more complex and include many other factors that may influence the generalization behavior of h_θ , such as training efficiency. Our theorem 1 provides a preliminary perspective to understand the model-level generalization error of h_θ .

4 Experiments

We then conduct experiments to verify the effectiveness of our proposed automatic weighting scheme for HSI denoising models. For convenience, the denoising models implemented with HWnet h_θ are prefixed by “HW-”.

4.1 Setting of source models

Three basic denoising models are used as source models to train HWnet. Their regularization term are nuclear norm NN (Zhang et al, 2013), spatial total variation norm (TV) (Zhang et al, 2019), and spectral total variation norm (TVS) (Zhang et al,

¹based on the approximate form of solution to denoising problem (2) because the optimization form itself is intractable to analysis.

2019). The NN can enforce the bands of HSI to lie in a low dimensional subspace, and the total variation regularization characterizes the smoothness property in the spatial and spectral dimensions. As reviewed in the related work section, such low-rank and spatial and spectral smoothness regularizers are the most commonly adopted ones in existing HSI denoising models. And they are also relatively easy to optimize. The ADMM (shown in Algorithm 1) is used to solve them due to its fast convergence and simple expression. Please see more algorithm details in Online Resource 1.

In the training framework (5a)-(5b), the above three denoising models can generate totally seven different combinations for the lower-level problem (5b) to train the HWnet, as listed in Table 2. The abbreviations “N”, “T” and “TS” mean using HW-NN, HW-TV and HW-TVS as single source model, respectively. The abbreviation “N+T” means that HW-NN and HW-TV are used to train the HWnet and thus the number of models T in (5b) is two. Consequently, we derive seven different HWnets under the seven different model combinations.

4.2 Details of training and testing data

To generate the training pairs, the CAVE dataset² (Yasuma et al, 2010) is used, which contains 32 images of real-world materials and objects. Specifically, we randomly select 20 images to generate the training pairs. The original size of each image is $512 \times 512 \times 31$, and we crop 2500 overlapping patches with a size of $64 \times 64 \times 31$. After rotating and flipping, the total number of training patch pairs is augmented to 20000. Additionally, seven HSI datasets are used for testing, including the remaining 10 images in the CAVE dataset, 10 images with a size of $512 \times 512 \times 31$ from ICVL dataset (Arad and Ben-Shahar, 2016), Washington DC Mall data³ with a size of $200 \times 200 \times 152$, PaviaU data⁴ with a size of $340 \times 340 \times 70$, Urban data (Kalman and Bassett III, 1997), Indian Pines data and a real HSI dataset⁵ in (Zhang et al,

2021). The first 4 testing datasets are used for synthetic HSI denoising experiments, and the last two datasets are used for real HSI denoising.

Firstly, we generate five kinds of complex noise for synthetic experiments. Note that only the noise in case 1 is used to generate the paired “clean/noisy” training patches. In the testing stage, the pairs generated by all five types of noise are used. The details of the generation process of noisy HSIs are as follows:

Case 1 (Gaussian + Impulse): Each band in HSI is corrupted with Gaussian noise, and the noise level is randomly selected from $[10,70]$. The number of selected bands with additional impulse noise are 10, 10, 40, and 20 for CAVE, ICVL, DC, and PaviaU, respectively. The ratio of impulse noise ranges from $[0.1,0.5]$.

Case 2 (Gaussian + Stripe): All the settings are the same as in Case 1, except that the stripe noise is substituted for the impulse noise. The ratio of the stripes ranges from $[0.05,0.2]$.

Case 3 (Gaussian + Deadline): All the settings are the same as in Case 1, except that the impulse noise is replaced by the deadline noise, the ratio of which ranges from $[0.05,0.2]$.

Case 4 (Spatial-Spectral Variant Gaussian): Each band of the HSI is corrupted with the spatial-spectral variant Gaussian noise. The noise level for each band is randomly generated by the normal distribution. The range of the noise level is between 10 and 70.

Case 5 (Mixture): The HSIs are corrupted with all the noise types from Case 1 to Case 4.

Four quantitative measures are used to evaluate the denoising performance, i.e., peak signal-to-noise ratio (PSNR), structural similarity (SSIM), spectral angle mapper (SAM), and erreur relative globale adimensionnelle de Synthèse (ERGAS). The ADAM (Kingma and Ba, 2014) is used to optimize the network parameters. The epoch number is set as 10. The initial learning rate is $1e^{-3}$ and decays by a factor of 0.8 every epoch. The batch size is set as 10. All the experiments are conducted on a PC with Intel Core i7-8700K CPU, and one GeForce RTX 2080 Ti with 11GB memory. It takes 4~6 hours to train each HWnet.

²<https://cave.cs.columbia.edu/repository/Multispectral>

³<https://engineering.purdue.edu/~biehl/MultiSpec/hyperspectral.html>

⁴https://www.ehu.es/ccwintco/index.php/Hyperspectral_Remote_Sensing_Scenes

⁵<https://github.com/ColinTaoZhang/HSIDwRD>

Table 2: All combinations of source models

source models ↓	corresponding trained HWnet (type)						
	N	T	TS	N+T	N+TS	T+TS	N+T+TS
HW-NN	✓			✓	✓		✓
HW-TV		✓		✓		✓	✓
HW-TVS			✓		✓	✓	✓

4.3 Weight visualization

It is evident that the implementation principle of HWnet is to extract a shared explicit weighting scheme across different noisy HSIs and diverse source models. This rationally makes it capable of capturing a unified weighting policy for general noisy HSIs with diverse noise types and different source models with diverse regularization terms. This implies that the extracted weight mapping from the trained HWnet for a testing HSI should beneficially deliver both its contained noise information and its possessed structural prior knowledge.

To intuitively illustrate this capability of HWnet, we visualize the predicted weights calculated by the seven different HWnets on a typical testing HSI in Fig. 4. Specifically, one band of the “watercolor” image in the CAVE dataset is corrupted with spatially non-i.i.d Gaussian noise, and the top-right area of the image is more heavily corrupted than the remaining areas. From the figure, the aforementioned analysis can be finely validated. Firstly, the heavy noise information located in the top-right area can be recognized by the weight predicted by all trained HWnets. The weight values in this noisy area are very small, meaning that all HWnets successfully recognize this polluted area and attempts to suppress its negative influence on the recovery by setting relatively smaller weights on it. Secondly, all generated weights from HWnet show evident structural shapes consistent with that of the ground-truth clean image. Especially, more important image structures for recovery, e.g., edges and textures, have been more emphasized by HWnet through specifying larger weights on them. Besides, the focus of image structures of each weight is also different, implying the underlying impact of different source models on the HWnet.

4.4 Application of HWnet

In this section, we select three popular HSI complex noise removal models as the target models for applying the trained HWnet. These models are LRTV (He et al, 2015b), E3DTV (Peng et al, 2020) and LRTFDFR (Zheng et al, 2020). Specifically, LRTV (He et al, 2015b) is a matrix-based method, which utilizes both spatial smoothness property and spectral low-rank property. E3DTV (Peng et al, 2020) is a tensor-based method that explores the sparsity of the base matrix of the gradient map in each mode. The loss functions of LRTV and E3DTV are both ℓ_1 norm. LRTFDFR (Zheng et al, 2020) employs the spectral low-rankness, the group sparsity on the gradient map of the base matrix, and the column continuity of the spectral factor matrix. The loss term of LRTFDFR includes both weighted ℓ_1 norm and ℓ_2 norm.

For each of the three target models, we modify it by simply replacing the loss term with $\|h_\theta(\mathcal{Y}) \odot (\mathcal{Y} - \mathcal{X})\|_2^2$. The modified models implemented with our HWnet are called HW-LRTV, HW-E3DTV and HW-LRTFDFR, respectively. They are also called *our* methods for convenience. In this section, the type-‘N+T+TS’ HWnet is applied for the three HW-models. Algorithms to solve the HW-models are inherited from the original model. More specifically HW-LRTV and HW-E3DTV are optimized by the ADMM algorithm which is also adopted in the original LRTV and E3DTV models. As for HW-LRTFDFR, we also adopt the ADMM algorithm because the proximal alternating minimization algorithm used by LRTFDFR can hardly be directly inherited. More details are presented in Online Resource 1.

We compare the three HW-methods with several advanced HSI complex noise removal methods including LRMR (Zhang et al, 2013), LRTV (He et al, 2015b), NMoG (Chen et al, 2017a), HyRes (Rasti et al, 2017), FastHyMix (Zhuang and Ng, 2021), CTV-RPCA (Peng et al, 2022b), E3DTV

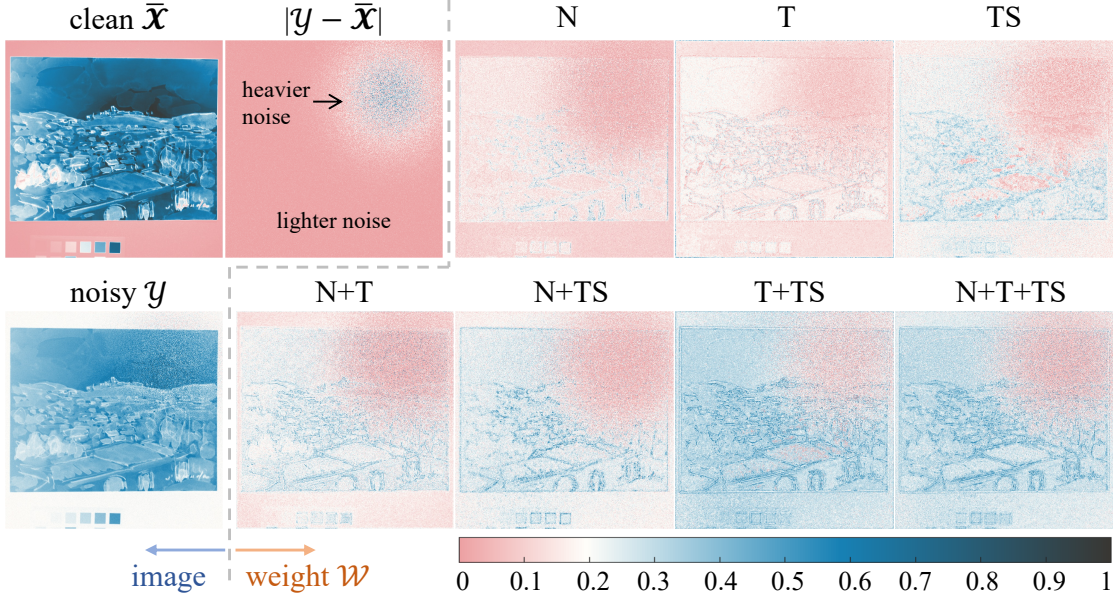


Fig. 4: Visual comparison of weight \mathcal{W} s predicted by different types of HWnet. There are two observations: 1) All the seven HWnets can recognize the heavier noise and assign smaller weights on this area, exactly showing the help-to-denoise function of HWnet. 2) HWnets additionally extract some image structures and the structures are different by different HWnets.

Table 3: Average test performance of different HSI denoising competing methods on the ICVL dataset. The best results in each **row** are in **bold**, and the second best results in each **row** are with underline.

noise \rightarrow	Case 1	Case 2	Case 3	Case 4	Case 5
index \rightarrow	PSNR/SSIM	PSNR/SSIM	PSNR/SSIM	PSNR/SSIM	PSNR/SSIM
LRMR	24.35/0.7214	27.77/0.8198	26.45/0.7962	26.15/0.7794	23/0.6868
LRTV	31.67/0.9059	32.91/0.9252	31.34/0.9135	35.49/0.9543	30.3/0.8971
NMoG	28.9/0.8718	30.32/0.9088	29.09/0.9013	26.68/0.8422	24.7/0.7553
HyRes	30/0.8829	35.09/0.9566	32.16/0.9308	32.25/0.9241	26.84/0.8357
FastHyMix	31.09/0.8914	37.30/0.9680	<u>34.19/0.9571</u>	36.23/0.961	27.9/0.8498
CTV-RPCA	31.09/0.8636	30.99/0.8579	30.37/0.8484	28.94/0.7944	28.45/0.7923
E3DTV	<u>34.61/0.9511</u>	34.27/0.9473	33.52/0.9425	32.88/0.9271	31.63/0.9154
LRTFDFR	29.69/0.8376	30.83/0.8479	27.92/0.7729	31.52/0.8553	28.42/0.8213
HSI-DeNet	29.33/0.8588	28.95/0.8389	28.39/0.8308	30.31/0.8843	28.37/0.842
HSI-CNN	34.36/0.932	<u>35.65/0.9551</u>	33.64/0.9456	37.38/0.9649	32.02/0.9206
HW-LRTV	34.94/0.9495	35.62/ <u>0.9593</u>	34.52/0.9523	<u>37.00/0.9692</u>	33.90/0.9480
HW-E3DTV	35.41/0.9529	35.46/0.959	35.20/0.9568	34.55/0.9476	33.26/0.9346
HW-LRTFDFR	34.09/0.9505	34.44/0.954	33.75/0.9464	35.42/0.964	<u>33.43/0.9469</u>

(Peng et al, 2020), LRTFDFR (Zheng et al, 2020), HSI-DeNet (Chang et al, 2018) and HSI-CNN (Yuan et al, 2018). The quantitative results are reported in Table 3. From the table, we can easily observe that our HWnet can dramatically improve the denoising results by comparing LRTV with

HW-LRTV or by comparing E3DTV with HW-E3DTV. Additionally, it can also be seen that our methods generally perform the best for different types of noise patterns even though only the noise in Case 1 is used in the training process. This verifies that the HWnet can learn a general weight

prediction rule for a wide range of complex noise types and thus can help the model to finely adapt to more noise types. Although FastHyMix achieves the best results in Case 2 (Gaussian+stripe), it does not perform well on the more complex noise in Case 5. We also compare our methods with all competing methods on one real noisy HSI dataset, Urban. The visual comparison is presented in Fig. 5. It can be observed that the restored HSI by our HW-E3DTV method can achieve the best visual result, while other competing methods do not fully remove the noise and the restored HSI always contains obvious blur effects or stripe noise. More experimental results are presented in Online Resource 1.

To further verify the ability of HWnet that can adjust weights for diverse complex noise types, we also compare our testing methods with several DL-based methods, i.e., T3SC (Bodrito et al, 2021), SST (Li et al, 2023a), SERT (Li et al, 2023b), on the real HSI dataset (Zhang et al, 2021). The results are presented in Table 4. We see that our testing methods could achieve comparable or even better performance than these supervised DL-based methods, although the DL-based methods require much more training sources.

From the above synthetic and real HSI denoising experiments, the effectiveness of our HWnet is reflected in two aspects. First, the trained HWnet helps boost the denoising performance of traditional HSI denoising models. It should be also noted that the HWnet is not limited to being used on the LRTV, E3DTV and LRTFDFR models, but could be plugged into general weighted HSI denoising models. Second, the HWnet inclines to learn a general weight prediction rule to help a model finely fit a wider range of noise types than those involved in HWnet training.

4.5 Model generalization analysis

In this section, we take a deeper step to explore how HWnet can behave between various source and target models.

4.5.1 Simple target models

In this experiment, we choose the target models exactly from the source models (i.e. HW-NN, HW-TV, and HW-TVS). Since the divergence between source and target models is relatively clear, we can

take a closer look at the generalization ability of all seven HWnets across different models.

The average experimental results on the ICVL dataset are shown in Table 5. The first row indexes seven types of HWnets, and the first column indexes the different noise types. For example, the ‘‘T’’ column means that the HWnet applied for the three target models is trained only using source model HW-TV. The quantitative results under five noise types are reported.

From Table 5, we can first observe that although the HWnet is trained only using the noise in Case 1, it can be finely generalized to other types of noises (Cases 2-5), which have not been seen during training. Besides, it seems that some HWnets always perform better on a specific target model. To explore the underlying rules, we compute the average PSNR value of all the five noise cases based on Table 5, and demonstrate the results in Table 6. Combining the two tables, we have the following observations. First, the corresponding HWnet inclines to perform the best when the source models and the target models match. For example, in Table 5, if the source model is ‘N’, the best denoising performance is obtained when the target model is HW-NN (see second column). The phenomena can also be seen from Table 6 whose diagonal values are the best. Second, the type-‘T’ HWnet does not generalize well to the other two models (i.e., ‘N’ and ‘TS’), while type-‘N’ HWnet generalizes better than the other two types of HWnet. Third, although the inconsistency between source and target models degrades the performance, the performance on the target models is still good enough. Fourth, when the number of target models grow, the performance also raises with the number of source models growing (see the last column of Table 6). This is because the HWnet can capture more regularization information from multiple source models.

We can also get more clues of Theorem 1 from Table 6. For convenience, we assume that the training error (first two terms of the upper bound) can be ignored. Denote the sum of the last two terms of the upper bound as

$$U(x, y) := \mathbb{E}_{(\mathcal{Y}, \mathcal{X}) \sim \mathcal{D}} \left\{ \frac{8B_d}{\sqrt{M}\varepsilon} A_1 \right\} +$$

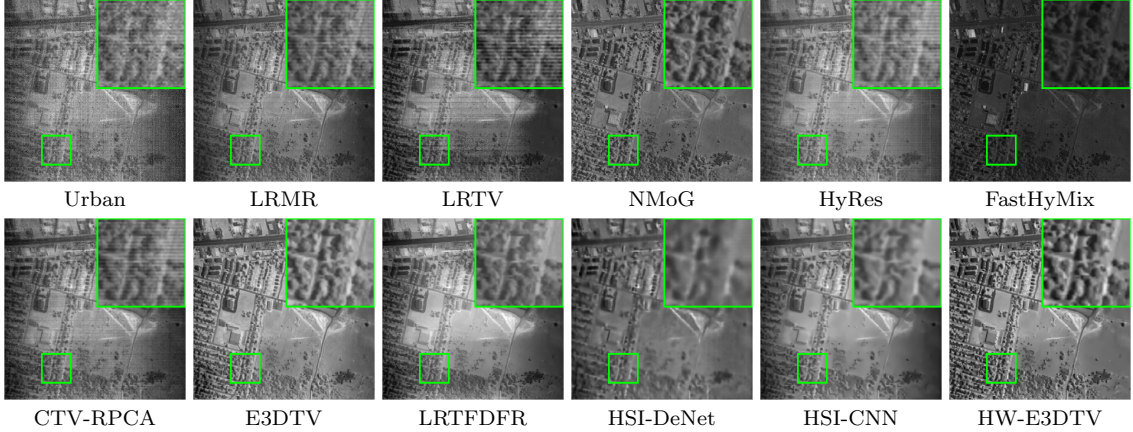


Fig. 5: Denoising results by different compared methods on the real noisy HSI Urban.

Table 4: Average results of T3SC, SST, SERT and our testing methods on the real HSI dataset (Zhang et al, 2021).

index	T3SC	SST	SERT	HW-LRTV	HW-E3DTV	HW-LRTFDFR
PSNR	29.19	29.29	28.97	29.5	<u>29.78</u>	29.82
SSIM	<u>0.9409</u>	0.9416	0.9377	0.929	0.9319	0.9358
SAM	2.50	3.02	3.13	<u>2.66</u>	3.07	2.98
ERGAS	126.16	128.51	132.01	124.42	<u>124.32</u>	119.61

$$\mathbb{E}_{(y,x) \sim D} \left\{ \frac{2}{M\epsilon^2} A_2 \right\}, \quad (11)$$

where $x = \{\text{source models}\}$, $y = \{\text{target models}\}$.

Then, a smaller $U(x, y)$ implies that the generalization error is more likely to be small. When source and target models are the same, we have $U(y, y) = 0$. Correspondingly, in Table 6, the diagonal results are generally the best since the source and target tasks exactly match. When the source and target models are different, there are also some relative observations. Let us first focus on the second column of Table 6. The target model is HW-NN. By the definition of U , we have $U(N+T, HW-NN) = \frac{1}{2}U(T, HW-NN)$ and $U(N+TS, HW-NN) = \frac{1}{2}U(TS, HW-NN)$. In Table 6, it also shows that the performance of ‘N+T’ is better than ‘T’ and ‘N+TS’ is better than ‘TS’. Besides, the performance of ‘TS’ is better than ‘T’, by which we may assume that $U(TS, HW-NN) < U(T, HW-NN)$ and thus $U(N+TS, HW-NN) < U(N+T, HW-NN)$. Correspondingly, Table 6 shows that the performance of

‘N+TS’ is better than ‘N+T’. More similar observations can be found for other source and target combinations in Table 6. It should be indicated that besides the intrinsics revealed by our learning theory, which inspires to understand the insightful working mechanism underlying our method, especially for its generalization ability, some other practical factors could also affect the generalization behaviour, such as training effectiveness. This is similar to the roles of the conventional learning theory results.

4.5.2 Complex target models

In this experiment, we apply the seven trained HWnets to LRTV (He et al, 2015b), E3DTV (Peng et al, 2020), and LRTFDFR (Zheng et al, 2020). The denoising results on the ICVL dataset are illustrated in Table 7. The second column of each sub-table (named “*Original”) in Table 7 records the performance of the original LRTV, E3DTV, and LRTFDFR models. Additionally, we also have the following observations from Table 7. Firstly, most models outperform their original

Table 5: Simple target models: average test performance of HW-NN, HW-TV and HW-TVS on ICVL dataset. The best results in each **row** are in **bold**, and the second best results in each **row** are with underline.

HWnet type →	N	T	TS	N+T	N+TS	T+TS	N+T+TS
index → noise ↓	PSNR/ SSIM	PSNR/ SSIM	PSNR/ SSIM	PSNR/ SSIM	PSNR/ SSIM	PSNR/ SSIM	PSNR/ SSIM
target model 1 : HW-NN							
Case 1	33.16/ 0.9452	22.44/ 0.6523	27.38/ 0.8348	32.53/ 0.9413	33.31 / <u>0.9440</u>	26.93/ 0.8292	32.93/ 0.9434
Case 2	<u>33.60</u> / <u>0.9493</u>	22.31/ 0.6449	27.80/ 0.8421	32.95/ 0.9431	33.71 / 0.9502	26.83/ 0.8257	33.35/ 0.9482
Case 3	<u>32.54</u> / 0.9461	22.37/ 0.6500	26.98/ 0.8320	31.80/ 0.9352	32.59 / <u>0.9433</u>	26.51/ 0.8228	32.16/ 0.9406
Case 4	32.39 / 0.9267	18.99/ 0.5332	25.09/ 0.7592	31.25/ 0.9138	<u>32.05</u> / <u>0.9253</u>	23.71/ 0.7321	31.54/ 0.9215
Case 5	30.43 / 0.9029	19.89/ 0.5492	23.90/ 0.7127	29.46/ 0.8907	<u>29.85</u> / <u>0.8950</u>	23.87/ 0.7287	29.61/ 0.8941
target model 2 : HW-TV							
Case 1	29.27/ 0.8355	32.84 / 0.9274	27.53/ 0.7872	31.52/ 0.8894	29.10/ 0.8343	<u>31.53</u> / <u>0.8898</u>	30.97/ 0.8757
Case 2	29.40/ 0.8459	32.95 / 0.9356	27.67/ 0.7935	<u>31.81</u> / <u>0.8987</u>	29.23/ 0.8461	31.72/ 0.8974	31.19/ 0.8862
Case 3	28.97/ 0.8385	31.94 / 0.9275	26.75/ 0.7762	<u>31.03</u> / <u>0.8916</u>	28.82/ 0.8372	30.76/ 0.8877	30.60/ 0.8793
Case 4	28.65/ 0.8272	31.38 / 0.9087	26.73/ 0.7695	<u>30.89</u> / <u>0.8807</u>	28.53/ 0.8283	30.80/ 0.8804	30.40/ 0.8697
Case 5	27.58/ 0.8003	29.67 / 0.8774	25.19/ 0.7229	<u>29.16</u> / <u>0.8555</u>	27.50/ 0.7985	28.97/ 0.8503	28.96/ 0.8427
target model 3 : HW-TVS							
Case 1	31.26/ 0.9125	24.17/ 0.6991	33.22 / 0.9249	30.49/ 0.9094	<u>32.35</u> / 0.9238	32.03/ <u>0.9241</u>	31.77/ 0.9240
Case 2	31.04/ 0.9135	23.97/ 0.6863	33.48 / 0.9292	30.22/ 0.9065	<u>32.34</u> / <u>0.9267</u>	32.08/ 0.9257	31.71/ 0.9253
Case 3	31.30/ 0.9151	24.05/ 0.6942	32.85 / <u>0.9243</u>	30.31/ 0.9060	<u>32.49</u> / 0.9260	31.59/ 0.9193	31.73/ 0.9239
Case 4	29.52/ 0.8833	21.30/ 0.5930	32.00 / 0.9041	28.67/ 0.8733	<u>30.96</u> / <u>0.9018</u>	30.54/ 0.8957	30.28/ 0.8981
Case 5	29.59/ 0.8711	21.88/ 0.6039	<u>30.47</u> / 0.8784	28.59/ 0.8599	30.60 / 0.8858	29.49/ 0.8723	29.84/ <u>0.8807</u>

models. This should be attributed to the powerful complex noise description ability of the loss term $\|h_\theta(\mathcal{Y}) \odot (\mathcal{Y} - \mathcal{X})\|_2^2$. Secondly, although only ‘‘Gaussian+impulse’’ noise is used for training the HWnet, the HW-models whose weight is predicted by the trained HWnet can also achieve superior results than the original models in other noise cases, which further proves the effectiveness of our HWnet to handle complex noise. This can be rationally explained by that our HWnet has learned the essential noise characteristics from the training data and thus can be well generalized to other noise types.

Table 8 averages the PSNR/SSIM results of all five noise cases. From Tables 7 and 8, we can observe that for HW-LRTV, the type-‘N+T+TS’ and type-‘N+T’ HWnets obtain the best and second best performance, which is reasonable since LRTV mainly considers the low-rankness and spatial smoothness property, complying with the ‘N’ regularization and ‘T’ regularization, respectively. As for HW-E3DTV and HW-LRTDFDR, the last two HWnets achieve the best results, which should be attributed to the fact that the HWnet learned from diverse models can generally capture more HSI priors, and thus can generalize well to a wide

Table 6: Average PSNR/SSIM values of all five kinds of noise patterns obtained by HW-NN, HW-TV and HW-TVS on ICVL dataset. The best results in each **column** are in **bold**, and the second best results in each **column** are with underline.

target → source ↓	HW-NN	HW-TV	HW-TVS	HW-NN & HW-TV	HW-NN & HW-TVS	HW-TV & HW-TVS	HW-NN & HW-TV & HW-TVS
N	32.42 / 0.9340	28.77/ 0.8295	30.54/ 0.8991	30.60/ 0.8818	31.48/ 0.9166	29.66/ 0.8643	30.58/ 0.8875
T	21.20/ 0.6059	31.76 / 0.9153	23.07/ 0.6553	26.48/ 0.7606	22.14/ 0.6306	27.41/ 0.7853	25.34/ 0.7255
TS	26.23/ 0.7962	26.77/ 0.7699	32.40 / <u>0.9122</u>	26.50/ 0.7830	29.32/ 0.8542	29.59/ 0.8410	28.47/ 0.8261
N+T	31.60/ 0.9248	<u>30.88</u> / <u>0.8832</u>	29.66/ 0.8910	31.24 / 0.9040	30.63/ 0.9079	30.27/ 0.8871	30.71/ <u>0.8997</u>
N+TS	<u>32.30</u> / <u>0.9316</u>	28.64/ 0.8289	<u>31.75</u> / 0.9128	30.47/ 0.8802	32.03 / 0.9222	30.19/ 0.8709	<u>30.90</u> / 0.8911
T+TS	25.57/ 0.7877	30.75/ 0.8811	31.14/ 0.9074	28.16/ 0.8344	28.36/ 0.8476	30.95 / 0.8943	29.16/ 0.8587
N+T+TS	31.92/ 0.9296	30.42/ 0.8707	31.07/ 0.9104	<u>31.17</u> / <u>0.9001</u>	<u>31.49</u> / <u>0.9200</u>	<u>30.75</u> / <u>0.8906</u>	31.14 / 0.9036

range of new target models. Additionally, we also notice that the type-‘T’ HWnet gains the lowest performance among the original and other models. The reason might be that the TV regularization only grabs the spatial features while neglecting the spectral correlation property, which has been verified to be of great importance for HSI denoising.

Further, Fig. 8 shows the visual comparison of the three new target models and their corresponding models with different HWnets. It can be easily seen that except for type-‘T’ HWnet, the proposed models with other HWnets can effectively remove the complex noise. For type-‘TS’ HWnet, some image details may be lost and the image always contains blurry boundaries. Additionally, the type-‘N+T+TS’ HWnet can achieve the best visual results.

We conducted a classification experiment on the Indian Pines dataset. The scene in this dataset contains 16 classes and the sample number of each class ranges from 20 to 2455. The classifier for this experiment is the basic support vector machine (SVM). For each class, we randomly select 15 samples for training and the remaining samples are used for testing. For each method, the experiment is conducted 10 times. The best result for each method is presented in Fig. 6. The overall accuracy is used to measure the classification results.

From Fig. 6, we can see that the denoised image of the model with the proposed weighting scheme achieves higher classification accuracy than that of its corresponding model, indicating that the proposed automatic weighting scheme can help improve the denoising performance.

We also compare our previous conference work (Rui et al, 2021) (named prev HWnet) with this work (named HWnet). The results are presented in Table 9. We can see that the performance of current HWnet outperforms that of prev HWnet in almost all cases for all three target models, which means that current HWnet can better adapt to diverse complex noise patterns and has better generalization ability than prev HWnet. This can be finely explained by two intrinsic aspects. First, we avoid the pre-assumption on the noise distribution required in the framework of prev HWnet and thus the HWnet can more flexibly learn how to generate weight. Second, we leverage diverse source models to train the HWnet so that it can be more adaptive to different target models. The overall performance shows that the weighting scheme in this work should work better than the previous version (Rui et al, 2021). More results are presented in Online Resource 1.

Table 7: Complex target models: average test performance of LRTV, E3DTV and LRTDFR and their corresponding HW-models on ICVL dataset. The best results in each **row** are in **bold**, and the second best results in each **row** are with underline.

HWnet type →	*Original (no h_θ)	N	T	TS	N+T	N+TS	T+TS	N+T +TS
index → noise ↓	PSNR/ SSIM	PSNR/ SSIM	PSNR/ SSIM	PSNR/ SSIM	PSNR/ SSIM	PSNR/ SSIM	PSNR/ SSIM	PSNR/ SSIM
target model 1 : LRTV								
Case 1	31.67/ 0.9059	34.44/ 0.9419	28.76/ 0.8152	31.45/ 0.9122	<u>34.54/</u> 0.9503	34.30/ 0.9417	34.31/ 0.9416	34.94/ <u>0.9495</u>
Case 2	32.91/ 0.9252	35.23/ 0.9538	29.23/ 0.8353	32.73/ 0.9275	<u>35.41/</u> <u>0.9592</u>	35.06/ 0.9542	35.05/ 0.9496	35.62/ 0.9593
Case 3	31.34/ 0.9135	34.21/ 0.9476	28.85/ 0.8301	31.01/ 0.9179	<u>34.22/</u> 0.9531	34.08/ 0.9462	33.57/ 0.9435	34.52/ <u>0.9523</u>
Case 4	35.49/ 0.9543	36.61/ 0.9645	32.25/ 0.9145	34.44/ 0.9520	<u>36.90/</u> 0.9709	36.59/ 0.9658	36.61/ 0.9686	37.00/ <u>0.9692</u>
Case 5	30.30/ 0.8971	<u>33.57/</u> 0.9418	28.94/ 0.8346	30.30/ 0.9102	33.34/ <u>0.9467</u>	33.55/ 0.9426	33.07/ 0.9432	33.90/ 0.9480
target model 2 : E3DTV								
Case 1	34.61/ 0.9511	34.97/ 0.9474	30.34/ 0.8741	34.37/ 0.9396	35.16/ 0.9563	34.95/ 0.9467	35.70/ <u>0.9551</u>	<u>35.41/</u> 0.9529
Case 2	34.27/ 0.9473	35.04/ 0.9532	29.76/ 0.8571	34.77/ 0.9474	35.18/ <u>0.9605</u>	35.10/ 0.9542	35.81/ 0.9613	<u>35.46/</u> 0.9590
Case 3	33.52/ 0.9425	35.06/ 0.9540	29.59/ 0.8591	33.53/ 0.9409	34.63/ 0.9570	<u>35.10/</u> 0.9529	34.83/ 0.9560	35.20/ <u>0.9568</u>
Case 4	32.88/ 0.9271	34.12/ 0.9420	27.81/ 0.7918	33.53/ 0.9331	34.13/ <u>0.9478</u>	34.19/ 0.9425	34.77/ 0.9492	<u>34.55/</u> 0.9476
Case 5	31.63/ 0.9154	33.21/ 0.9307	27.75/ 0.7888	31.15/ 0.9110	32.61/ <u>0.9337</u>	33.23/ 0.9300	32.77/ 0.9318	33.26/ 0.9346
target model 3 : LRTDFR								
Case 1	29.69/ 0.8376	33.63/ 0.9421	27.97/ 0.8116	32.03/ 0.9224	33.70/ <u>0.9506</u>	33.81/ 0.9444	34.16/ 0.9526	<u>34.09/</u> 0.9505
Case 2	30.83/ 0.8479	34.21/ 0.9496	28.66/ 0.8374	32.82/ 0.9287	34.17/ 0.9523	34.03/ 0.9491	34.56/ <u>0.9525</u>	<u>34.44/</u> 0.9540
Case 3	27.92/ 0.7729	33.25/ 0.9402	28.29/ 0.8267	31.25/ 0.9064	33.10/ 0.9418	33.37/ 0.9406	<u>33.43/</u> <u>0.9426</u>	33.75/ 0.9464
Case 4	31.52/ 0.8553	35.41/ 0.9617	31.12/ 0.9096	34.70/ 0.9534	35.23/ 0.9642	35.23/ 0.9614	35.51/ 0.9630	<u>35.42/</u> <u>0.9640</u>
Case 5	28.42/ 0.8213	33.00/ 0.9382	28.41/ 0.8340	31.61/ 0.9248	32.70/ 0.9436	33.22/ 0.9413	<u>33.22/</u> 0.9475	33.43/ <u>0.9469</u>

4.5.3 Special target models: deep image prior

As mentioned in Sec. 3.2.1, deep image prior problem of form (8) can be seen as a special kind of target models. In this experiment, we use S2DIP (Luo et al, 2021) as the backbone model since it is specifically designed for HSI denoising.

Table 10 shows the experimental results on the CAVE dataset in five noise cases. Each restoration experiment is repeated 3 times and the average results are recorded. In Table 10, the “max” column presents the maximum output PSNR value

during training. The “final” column means the average PSNR values of the last 100 iterations, and also represents the converged results. “|d.v|” is the absolute difference value between the maximum and the final values. From Table 10, we can see that the HW-S2DIP model outperforms the original model in most noise cases. For example, most of the HW-S2DIP models perform better than the original model in the complex noise case (i.e., Case 5). Besides, the “|d.v|” value of the HW-S2DIP model is always smaller than S2DIP, which reveals that the HW-S2DIP models are

Table 8: Average PSNR/SSIM values of all five kinds of noise patterns obtained by LRTV, E3DTV, LRTFDFR and their corresponding HW-models on ICVL dataset.

target models → HWnet type ↓	LRTV	E3DTV	LRTFDFR
<i>*Original</i>	32.34/0.9192	33.38/0.9367	29.68/0.827
N	34.81/0.9499	34.48/0.9455	33.9/0.9464
T	29.61/0.8459	29.05/0.8342	28.89/0.8439
TS	31.99/0.924	33.47/0.9344	32.48/0.9271
N+T	<u>34.88/0.9560</u>	34.34/0.9511	33.78/0.9505
N+TS	34.72/0.9501	34.51/0.9453	33.93/0.9474
T+TS	34.52/0.9493	<u>34.78/0.9507</u>	<u>34.18/0.9516</u>
N+T+TS	35.20/0.9557	34.78/0.9502	34.23/0.9524

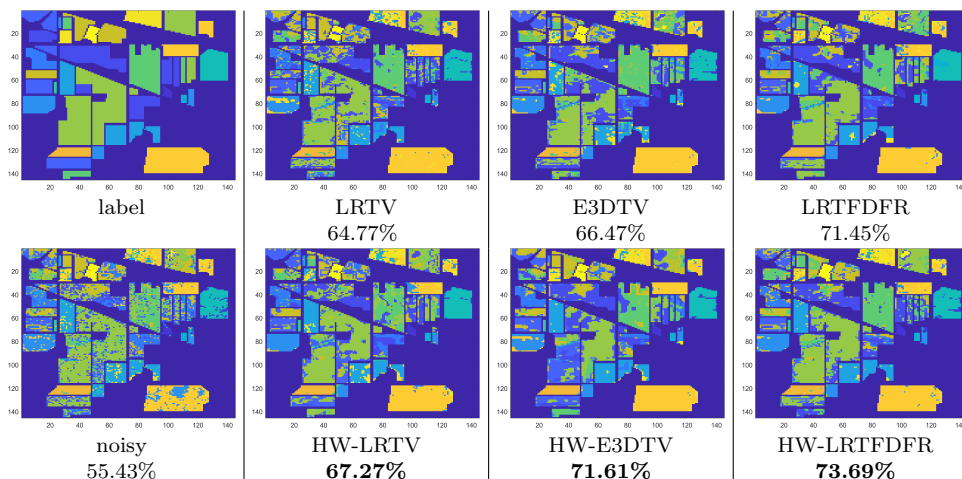


Fig. 6: Classification results of the compared methods on the Indian Pines dataset.

more stable than the original model. A different observation from previous experiments is that the type-‘T’ HWnet doesn’t perform the worst among all HWnets. This is perhaps due to the extra implicit image prior brought by network g_η . Fig. 9 shows the visual comparison of S2DIP and HW-S2DIP in Case 3. We can see that the deadline noise is not completely removed by S2DIP, while most of the HW-S2DIP models achieve better visual results. To illustrate the convergence, we also plot the PSNR tendency during the training process in Fig. 7. Except for type-‘TS’ HWnet, HW-S2DIP with other HWnets converges very quickly in the early stage. In Case 5, we see that the HW-S2DIP with type-‘N+T+TS’ HWnet suffers from one big vibration at about the 6000th iteration, which causes a large “|d.v|” value 0.424 in Table 10. However, its performance keeps rising after the 6000th iteration and finally reaches the third best.

5 Limitations

The proposed automatic weighting scheme still has several limitations. Firstly, the learning of the HWnet requires the iterative optimization algorithm of solving the lower-level problem to be differentiable w.r.t. weight \mathcal{W} . However, some common operators only have sub-gradients, such as nuclear norm and total variation (TV) norm, which may make the training of HWnet unstable. Secondly, the theoretical analysis of generalization error is based on an approximation to the solution to the source models. Besides, the source and target models are symmetric in $U(x, y)$, i.e., $U(x, y) = U(y, x)$. However, in practice it could be different when exchanging the source and target tasks. For example, Table 6 shows that the performance of applying type-‘N’ HWnet to HW-TV is different from applying type-‘T’ HWnet to HW-NN. Thus there still exists some gap in

Table 9: Average PSNR/SSIM results of prev HWnet by (Rui et al, 2021) and HWnet of this work on ICVL dataset. The target models are LRTV, E3DTV and LRTFDFR.

noise ↓	target →	LRTV	E3DTV	LRTFDFR
case 1	prev HWnet	30.84/0.9041	32.56/0.9199	31.69/0.9145
	HWnet (this work)	34.94/0.9495	35.41/0.9529	34.09/0.9505
case 2	prev HWnet	34.02/0.9504	35.43/0.9551	34.73/0.9520
	HWnet (this work)	35.62/0.9593	35.46/0.9590	34.44/0.9540
case 3	prev HWnet	32.46/0.9474	34.51/0.9518	33.34/0.9430
	HWnet (this work)	34.52/0.9523	35.20/0.9568	33.75/0.9464
case 4	prev HWnet	35.49/0.9607	34.30/0.9432	36.01/0.9645
	HWnet (this work)	37.00/0.9692	34.55/0.9476	35.42/0.9640
case 5	prev HWnet	30.59/0.9113	31.04/0.8996	31.98/0.9305
	HWnet (this work)	33.90/0.9480	33.26/0.9346	33.43/0.9469

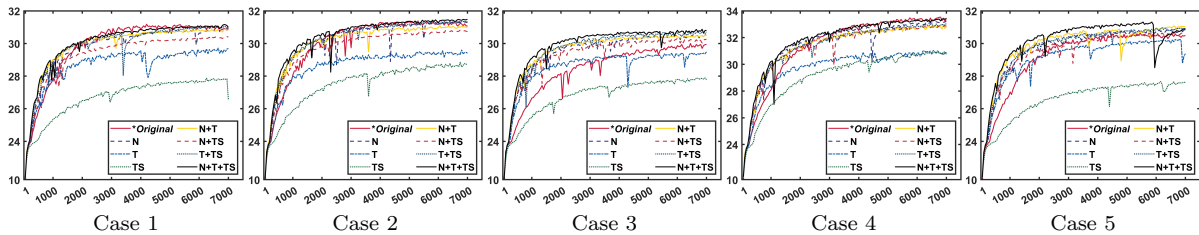


Fig. 7: The tendency of PSNR values during iterations for S2DIP and HW-S2DIP with different HWnets.

fully understanding the generalization behavior of HWnet. Additionally, how to further improve the generalization ability of HWnet still needs to be more deeply and comprehensively investigated. Some possible strategies may help, such as constraining specific structures on the predicted parameters (Shu et al, 2021). Furthermore, we will consider ways to address and incorporate more physical insights underlying HSIs noise to further improve the quality of our extracted weighting scheme and enhance its denoising effect. We will investigate these issues in our future research.

6 Conclusion

In this work, we have proposed an automatic weighting scheme for the weighted HSI denoising models. The weight is predicted by an explicit neural network mapping called HWnet, which can be learned under a bi-level optimization framework. The trained HWnet has been validated to be able to generalize to other weighted HSI denoising models in a plug-and-play manner. Experimental results have substantiated that the proposed HWnet can help a new weighted HSI denoising model to finely adapt to complex noise types

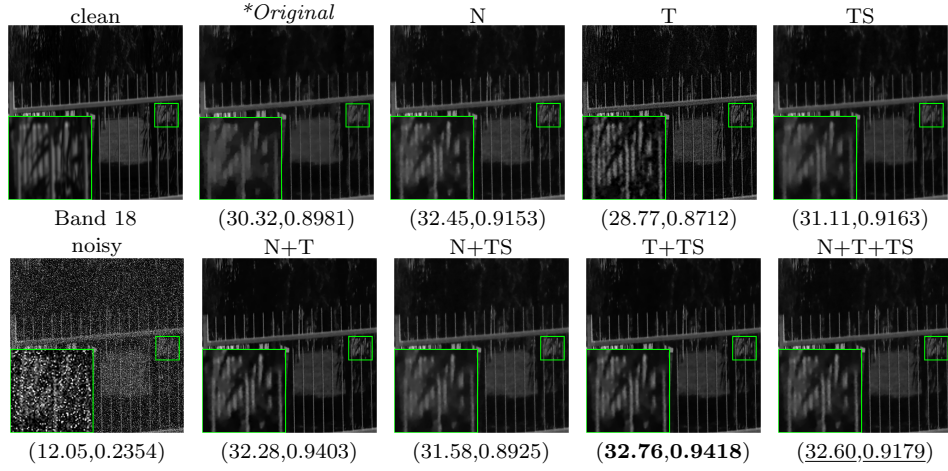
and thus can generalize well to different HSI datasets. Also, experimental results validated that the HWnet trained with diverse regularizers (i.e., models) can be used for new models to further improve their denoising performance. Additionally, we have further theoretically proved a generalization error upper bound of the HWnet when it is plugged into a new weighted denoising model, showing its insightfully possessed generalization capability.

Statements and declarations

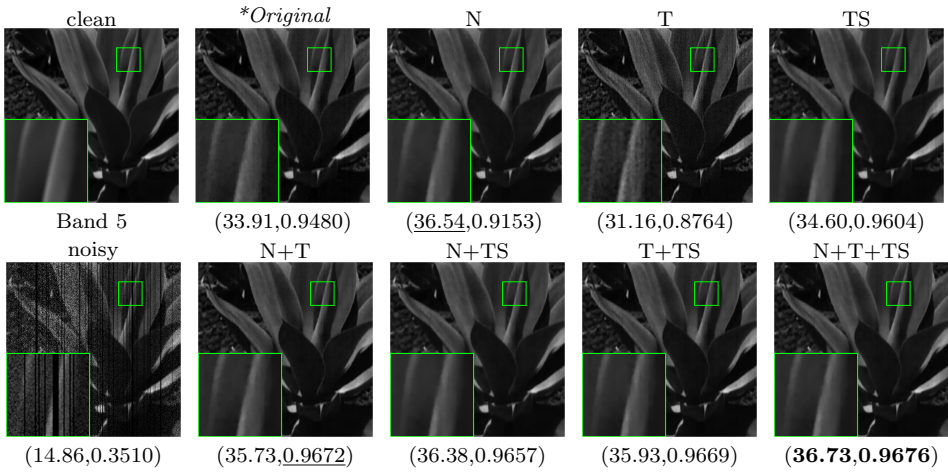
Competing Interests.: The authors declare that they have no Conflict of interest.

Supplementary information. A few supplementary files are attached:

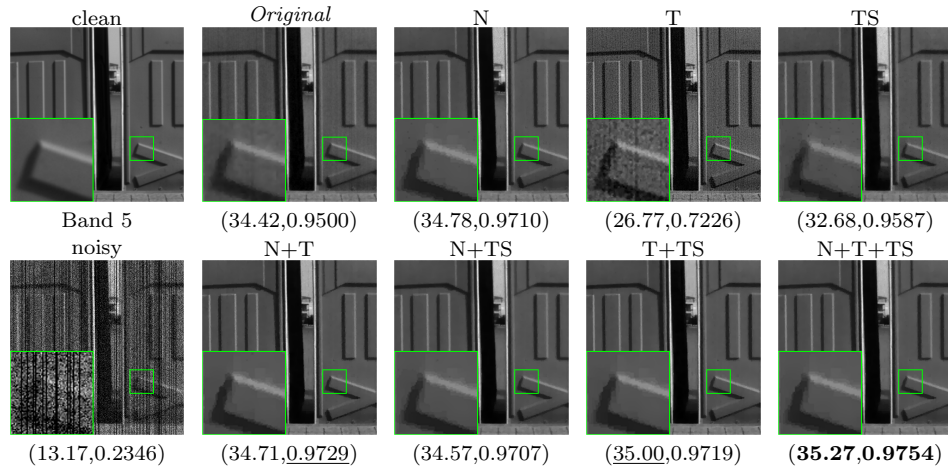
- Online Resource 1 (Supp): This file includes details about algorithms and more experimental results about this work.
- Online Resource 2 (Difference): This file states detailed differences between this work and our previous conference work.
- Online Resource 3 (Conference): This is our previous conference work.



(a) target model: LRTV



(b) target model: E3DTV



(c) target model: LRTFDFR

Fig. 8: Denoising results of LRTV, E3DTV, LRTFDFR and their corresponding HW-models on ICVL dataset. From top to bottom, noisy HSIs are corrupted with “Gaussian+impulse”, “mixture” and “Gaussian+deadline” noise patterns.

Table 10: PSNR results of “jelly_beans” in CAVE dataset for S2DIP and HW-S2DIP with different HWnets. The best results in each **column** are in **bold**, and the second best results in each **column** are with underline.

HWnet type →		target model: S2DIP							
		<i>*Original</i> (no h_θ)	N	T	TS	N+T	N+TS	T+TS	N+T +TS
Case 1	max	31.20	30.95	29.85	27.94	30.93	30.46	31.1	<u>31.16</u>
	final	30.91	30.87	29.62	27.48	30.84	30.37	<u>31.02</u>	31.09
	d.v	0.282	0.074	0.232	0.461	0.088	0.095	0.078	<u>0.076</u>
Case 2	max	31.41	31.35	29.63	28.9	31.11	30.85	<u>31.43</u>	31.54
	final	31.18	31.28	29.41	28.72	31.02	30.77	<u>31.34</u>	31.45
	d.v	0.229	0.076	0.226	0.176	0.087	0.083	0.09	<u>0.081</u>
Case 3	max	30.13	30.6	29.5	27.96	30.58	30.35	<u>30.80</u>	30.87
	final	29.89	30.47	29.37	27.83	30.45	30.22	<u>30.67</u>	30.78
	d.v	0.231	0.137	0.125	0.139	<u>0.123</u>	0.13	0.131	0.097
Case 4	max	33.60	33.26	31.18	31.05	32.99	32.94	33.1	<u>33.48</u>
	final	33.44	33.17	30.89	30.92	32.83	32.86	33	<u>33.37</u>
	d.v	0.155	<u>0.092</u>	0.29	0.13	0.165	0.085	0.096	0.117
Case 5	max	30.67	30.94	30.31	27.72	<u>31.12</u>	30.74	31.02	31.33
	final	30.43	30.8	29.48	27.62	31.03	30.62	30.9	<u>30.91</u>
	d.v	0.242	0.145	0.831	<u>0.100</u>	0.092	0.125	0.113	0.424

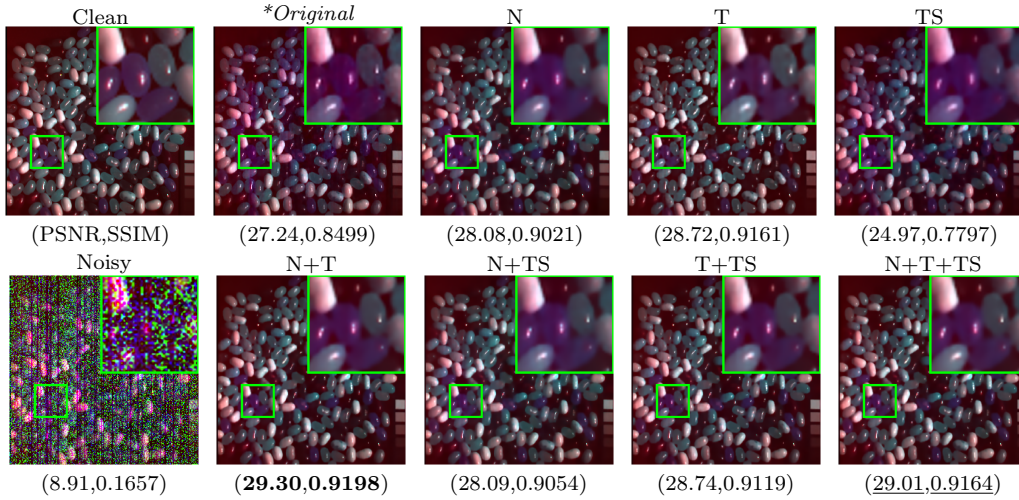


Fig. 9: Visual comparison of S2DIP and HW-S2DIP with different HWnets of “jelly_beans” in CAVE dataset. The PSNR and SSIM measures are shown below each restored image for easy observation.

Data availability statements.

- The CAVE dataset is available at <https://cave.cs.columbia.edu/repository/Multispectral>.
- The ICVL dataset is available at https://doi.org/10.1007/978-3-319-46478-7_2.
- The Washington DC Mall is available at <https://engineering.purdue.edu/~biehl/MultiSpec/hyperspectral.html>.
- The PaviaU is available at https://www.ehu.es/ccwintco/index.php/Hyperspectral_Remote_Sensing_Scenes.
- The Urban is available at <https://doi.org/10.1117/12.283843>.
- The Indian Pines data is available at https://www.ehu.es/ccwintco/index.php/Hyperspectral_Remote_Sensing_Scenes.
- Realistic hyperspectral dataset is available at <https://doi.org/10.1007/s11263-022-01660-2>.

Appendix A Details about Algorithm 1

Algorithm 1 shows how to apply ADMM to solve the denoising problem (2). Specifically, denoising problem has the following form

$$\min_{\mathcal{X}} \frac{1}{2} \|\mathcal{W} \odot (\mathcal{Y} - \mathcal{X})\|_2^2 + \lambda R(\mathcal{X}). \quad (\text{A1})$$

To solve this problem, we first introduce an auxiliary variable \mathcal{Z} , and transform the above problem into the following consensus form

$$\begin{aligned} \min_{\mathcal{X}, \mathcal{Z}} \frac{1}{2} \|\mathcal{W} \odot (\mathcal{Y} - \mathcal{Z})\|_2^2 + \lambda R(\mathcal{X}), \\ \text{s.t. } \mathcal{X} = \mathcal{Z}. \end{aligned} \quad (\text{A2})$$

The corresponding augmented Lagrangian is

$$\begin{aligned} L(\mathcal{X}, \mathcal{Z}, \Gamma) = \frac{1}{2} \|\mathcal{W} \odot (\mathcal{Y} - \mathcal{Z})\|_2^2 \\ + \lambda R(\mathcal{X}) + \langle \Gamma, \mathcal{X} - \mathcal{Z} \rangle + \frac{\mu}{2} \|\mathcal{X} - \mathcal{Z}\|_2^2, \end{aligned} \quad (\text{A3})$$

The updating rules of ADMM is written as

$$\begin{cases} \mathcal{X} \leftarrow \arg \min_{\mathcal{X}} L(\mathcal{X}, \mathcal{Z}, \Gamma), & (\text{A4a}) \\ \mathcal{Z} \leftarrow \arg \min_{\mathcal{Z}} L(\mathcal{X}, \mathcal{Z}, \Gamma), & (\text{A4b}) \\ \Gamma \leftarrow \Gamma + \mu(\mathcal{X} - \mathcal{Z}). & (\text{A4c}) \end{cases}$$

Problems in (A4a) and (A4b) are called \mathcal{X} - and \mathcal{Z} - subproblems, respectively. The \mathcal{X} -subproblem has the specific form of

$$\begin{aligned} \arg \min_{\mathcal{X}} \frac{\mu}{2} \left\| \mathcal{X} - \left(\mathcal{Z} - \frac{\Gamma}{\mu} \right) \right\|_2^2 + \lambda R(\mathcal{X}), \quad (\text{A5}) \\ = \text{prox}_{\frac{\lambda}{\mu} R} \left(\mathcal{Z} - \frac{\Gamma}{\mu} \right). \end{aligned}$$

The \mathcal{X} -subproblem may not have closed-form solution, which depends on the choice of $R(\cdot)$. The \mathcal{Z} -subproblem has the specific form of

$$\begin{aligned} \arg \min_{\mathcal{Z}} \frac{1}{2} \|\mathcal{W} \odot (\mathcal{Y} - \mathcal{Z})\|_2^2 + \frac{\mu}{2} \left\| \mathcal{Z} - \left(\mathcal{X} + \frac{\Gamma}{\mu} \right) \right\|_2^2, \\ = \frac{\mathcal{W}^2 \odot \mathcal{Y} + \mu \mathcal{X} + \Gamma}{\mathcal{W}^2 + \mu}. \end{aligned} \quad (\text{A6})$$

Note that the \mathcal{Z} -subproblem has the closed form solution.

Appendix B Details about Theory

To build the theoretical analysis, we first replenish the bi-level learning framework proposed in (5a)-(5b). Then, we provide a training error estimation to clarify that each HSI denoising model contributes to the final training performance. Next, we prove a generalization error upper bound of our proposed HWnet to illuminate its intrinsic model generalization capability.

B.1 Preparation

Let data space \mathbb{Y} and \mathbb{X} denote the degraded image space and the clean image space, respectively. We have that $\mathcal{Y} \in \mathbb{Y}$ and $\mathcal{X} \in \mathbb{X}$. Denote M as the size $h * w * b$, and we assume that $\mathbb{Y} \subseteq \mathbb{R}^M$ and $\mathbb{X} \subseteq \mathbb{R}^M$. Furthermore, \mathbb{Y} and \mathbb{X} should be considered to be bounded since the clean images are usually normalized in the pre-processing step. Although the additive random noise is unbounded theoretically, the intensity of an observed noisy image \mathcal{Y} should be limited in real cases. Therefore, we assume that both \mathbb{Y} and \mathbb{X} are bounded sets in \mathbb{R}^M , which is summarized as follows:

Assumption 1. $|\mathcal{Y}| \leq B_d, |\mathcal{X}| \leq B_d, \forall \mathcal{Y} \in \mathbb{Y}, \forall \mathcal{X} \in \mathbb{X}$.

Let D represent a joint distribution defined on $\mathbb{Y} \times \mathbb{X}$. To be specific, the joint probability density function (PDF) $p(\mathcal{Y}, \mathcal{X})$ is usually decomposed as

$$p(\mathcal{Y}, \mathcal{X}) = p(\mathcal{Y}|\mathcal{X})p(\mathcal{X}),$$

where $p(\mathcal{X})$ represents the PDF of the clean data \mathcal{X} , and $p(\mathcal{Y}|\mathcal{X})$ reveals the generative process of noisy data \mathcal{Y} conditioned on \mathcal{X} ⁶. The training data $(\mathcal{Y}, \bar{\mathcal{X}})$ s are all i.i.d sampled from D .

We firstly prove a Lemma that clarifies the implicit mapping from \mathcal{W} to $\hat{\mathcal{X}}$ as follows.

Lemma 1. *Suppose $\mathcal{W} \geq \varepsilon > 0$ and R is a proper closed and convex function, then the solution to the problem (2) is unique.*

Proof. Let $f_1(\mathcal{X}) := \frac{1}{2}\|\mathcal{W} \odot (\mathcal{Y} - \mathcal{X})\|_2^2$. For any $\eta \in [0, 1]$, we have that

$$\begin{aligned} & \eta f_1(\mathcal{X}) + (1 - \eta)f_1(\mathcal{Z}) - f_1(\eta\mathcal{X} + (1 - \eta)\mathcal{Z}) \\ &= \frac{\eta}{2}\|\mathcal{W} \odot \mathcal{X}\|_2^2 + \frac{1 - \eta}{2}\|\mathcal{W} \odot \mathcal{Z}\|_2^2 \\ & \quad - \frac{1}{2}\|\mathcal{W} \odot (\eta\mathcal{X} + (1 - \eta)\mathcal{Z})\|_2^2 \\ &= \frac{1}{2}\eta(1 - \eta)\|\mathcal{W} \odot (\mathcal{X} - \mathcal{Z})\|_2^2 \\ & \geq \frac{\varepsilon^2}{2}\eta(1 - \eta)\|\mathcal{X} - \mathcal{Z}\|_2^2. \end{aligned}$$

Thus, $f_1(\mathcal{X})$ is a ε^2 -strongly convex function. Similar to Theorem 6.3 in (Beck, 2017), the objective function in (2) is a proper closed and strongly convex function. Thus the solution to (2) is unique. \square

Based on Lemma 1, we can also define the solution of problem (2) explicitly as follows:

$$f_{\lambda R}^h(\mathcal{Y}; \theta) := \arg \min_{\mathcal{X}} \frac{1}{2}\|h_\theta(\mathcal{Y}) \odot (\mathcal{Y} - \mathcal{X})\|_2^2 + \lambda R(\mathcal{X}), \quad (\text{B7})$$

which has an equivalent meaning to $\hat{\mathcal{X}}(\mathcal{Y}, \theta, R)$ defined in (4). We continue to call “ $f_{\lambda R}^h$ ” a source model. The T source models $\{f_{\lambda_t R_t}^h\}_{t=1}^T$ in the lower level problem (5b) can be aggregated into

$$\mathcal{F}_{\mathcal{H}} := \{(f_{\lambda_1 R_1}^h, \dots, f_{\lambda_T R_T}^h) | h \in \mathcal{H}\}.$$

⁶Here, we do not distinguish the variable “ \mathcal{X} ” from a sample “ \mathcal{X} ”.

We call $\mathcal{F}_{\mathcal{H}}$ the source model set since it includes all denoising models for training h_θ . \mathcal{H} is the hypothesis set that contains all possible h_θ captured by θ . Despite the distinction of denoising models in $\mathcal{F}_{\mathcal{H}}$, the purposes of weighting are the same, i.e. leveraging noise information for better denoising. In Sec. B.2, we first provide the training error. Then, we will discuss the generalization ability of h_θ at the model level.

B.2 Training Error Estimation

Since $\hat{\mathcal{X}}_{ti_t} = f_{\lambda_t R_t}^h(\mathcal{Y}_{ti_t})$, the upper level problem (5a) can be equivalently written as

$$\min_{h \in \mathcal{H}} \frac{1}{T} \sum_{t=1}^T \frac{1}{N_t} \sum_{i_t=1}^{N_t} \ell_{net}(f_{\lambda_t R_t}^h(\mathcal{Y}_{ti_t}), \bar{\mathcal{X}}_{ti_t}). \quad (\text{B8})$$

Here, we use ℓ_{net} to represent a general form of the training loss. It is obvious that Eq. (B8) can be regarded as the *empirical risk minimization* (ERM) (Mohri et al, 2018) of $h \in \mathcal{H}$ on samples $\mathbf{S} = \{(\mathcal{Y}_{ti_t}, \bar{\mathcal{X}}_{ti_t})\}_{i_t=1}^{N_t} \}_{t=1}^T$. Therefore, our training loss, or empirical risk, refers to

$$\hat{\mathbf{R}}_{tr}(h) := \frac{1}{T} \sum_{t=1}^T \frac{1}{N_t} \sum_{i_t=1}^{N_t} \ell_{net}(f_{\lambda_t R_t}^h(\mathcal{Y}_{ti_t}), \bar{\mathcal{X}}_{ti_t}).$$

And the expected risk is

$$\mathbf{R}_{tr}(h) := \frac{1}{T} \sum_{t=1}^T \mathbb{E}_{(\mathcal{Y}, \mathcal{X}) \sim D} [\ell_{net}(f_{\lambda_t R_t}^h(\mathcal{Y}), \mathcal{X})].$$

The expected risk takes expectations over joint distribution D . Correspondingly, the “best HWnet”s are defined as:

$$\begin{aligned} \hat{h}_{tr} &:= \arg \min_{h \in \mathcal{H}} \hat{\mathbf{R}}_{tr}(h), \\ h_{tr}^* &:= \arg \min_{h \in \mathcal{H}} \mathbf{R}_{tr}(h), \end{aligned}$$

where \hat{h}_{tr} is the final trained HWnet under the bi-level framework (5a)-(5b) with a finite set of training samples, and h_{tr}^* is the ideal HWnet which is calculated from the underlying sample distribution D . Since the expected h_{tr}^* is intractable, the training error \mathbf{E}_{tr} to measure the “closeness” between \hat{h}_{tr} and h_{tr}^* is then defined as:

$$\mathbf{E}_{tr} := \mathbf{R}_{tr}(\hat{h}_{tr}) - \mathbf{R}_{tr}(h_{tr}^*). \quad (\text{B9})$$

Next, our goal is to estimate the upper bound of \mathbf{E}_{tr} . To achieve this goal, we first need to present some properties and assumptions on the hypothesis set \mathcal{H} and source model set $\mathcal{F}_{\mathcal{H}}$, which is shown as follows:

Lemma 2. *Let $h_1, h_2 \in \mathbb{R}^M$ and $0 < \varepsilon \leq h_1, h_2 \leq B_H$. R is convex and closed and has subgradients. Then $\forall \mathcal{Y} \in \mathbb{Y}$, we have*

$$\|f_R^{h_1}(\mathcal{Y}) - f_R^{h_2}(\mathcal{Y})\|_2 \leq L_H \|h_1 - h_2\|_2. \quad (\text{B10})$$

The Lipschitz constant L_H only depends on B_d , ε and B_H .

Proof. Let $\mathcal{X}_1 = f_{\lambda R}^{h_1}(\mathcal{Y})$ and $\mathcal{X}_2 = f_{\lambda R}^{h_2}(\mathcal{Y})$. According to the definition of $f_{\lambda R}^h$, we have that

$$\mathcal{X}_1 = \arg \min_{\mathcal{X}} \frac{1}{2} \|h_1 \odot (\mathcal{Y} - \mathcal{X})\|_2^2 + \lambda R(\mathcal{X}),$$

$$\mathcal{X}_2 = \arg \min_{\mathcal{X}} \frac{1}{2} \|h_2 \odot (\mathcal{Y} - \mathcal{X})\|_2^2 + \lambda R(\mathcal{X}).$$

Since R has subgradients, then we have

$$h_1^2 \odot (\mathcal{X}_1 - \mathcal{Y}) + \lambda \partial R(\mathcal{X}_1) = 0,$$

$$h_2^2 \odot (\mathcal{X}_2 - \mathcal{Y}) + \lambda \partial R(\mathcal{X}_2) = 0.$$

Since R is convex, according to

$$R(x) - R(y) \geq \langle \partial R(y), x - y \rangle,$$

we have

$$R(\mathcal{X}_2) - R(\mathcal{X}_1) \geq \langle \partial R(\mathcal{X}_1), \mathcal{X}_2 - \mathcal{X}_1 \rangle,$$

$$R(\mathcal{X}_1) - R(\mathcal{X}_2) \geq \langle \partial R(\mathcal{X}_2), \mathcal{X}_1 - \mathcal{X}_2 \rangle.$$

Combining the above two equations, we get

$$\begin{aligned} & \langle \partial R(\mathcal{X}_2) - \partial R(\mathcal{X}_1), \mathcal{X}_1 - \mathcal{X}_2 \rangle \leq 0, \\ \Rightarrow & \left\langle \frac{h_2^2}{\lambda} \odot (\mathcal{Y} - \mathcal{X}_2) - \frac{h_1^2}{\lambda} \odot (\mathcal{Y} - \mathcal{X}_1), \mathcal{X}_1 - \mathcal{X}_2 \right\rangle \leq 0, \\ \Rightarrow & \langle h_1^2 \odot \mathcal{X}_1 - h_2^2 \odot \mathcal{X}_2, \mathcal{X}_1 - \mathcal{X}_2 \rangle \\ & \leq \langle \mathcal{Y} \odot (h_1^2 - h_2^2), \mathcal{X}_1 - \mathcal{X}_2 \rangle \\ \Rightarrow & \langle h_1^2 \odot (\mathcal{X}_1 - \mathcal{X}_2), \mathcal{X}_1 - \mathcal{X}_2 \rangle \\ & \leq \langle (\mathcal{Y} - \mathcal{X}_2) \odot (h_1^2 - h_2^2), \mathcal{X}_1 - \mathcal{X}_2 \rangle. \end{aligned} \quad (\text{B11})$$

For the left side of Eq. (B11), we have

$$\langle h_1^2 \odot (\mathcal{X}_1 - \mathcal{X}_2), \mathcal{X}_1 - \mathcal{X}_2 \rangle \geq \varepsilon^2 \|\mathcal{X}_1 - \mathcal{X}_2\|_2^2 \geq 0.$$

Thus,

$$\begin{aligned} & \varepsilon^2 \|\mathcal{X}_1 - \mathcal{X}_2\|_2^2 \leq \langle (\mathcal{Y} - \mathcal{X}_2) \odot (h_1^2 - h_2^2), \mathcal{X}_1 - \mathcal{X}_2 \rangle \\ & \leq \langle (\mathcal{Y} - \mathcal{X}_2) \odot (h_1^2 - h_2^2), \mathcal{X}_1 - \mathcal{X}_2 \rangle \\ & \leq \|(\mathcal{Y} - \mathcal{X}_2) \odot (h_1^2 - h_2^2)\|_2 \|\mathcal{X}_1 - \mathcal{X}_2\|_2 \\ & \leq \|(\mathcal{Y} - \mathcal{X}_2) \odot (h_1 - h_2) \odot (h_1 + h_2)\|_2 \\ & \leq L_H \|h_1 - h_2\|_2. \end{aligned}$$

The proof is then completed. \square

Lemma 2 shows the Lipschitz continuity of f_R^h w.r.t. weight h , which means that if two input weights h_1 and h_2 are close enough, the corresponding restored images $f_R^{h_1}(\mathcal{Y})$ and $f_R^{h_2}(\mathcal{Y})$ are also close. Furthermore, a mild assumption is made on \mathcal{H} , which is shown as

Assumption 2. $0 < \varepsilon \leq h \leq B_H, \forall h \in \mathcal{H}$.

Based on the Lemma 2 and the Assumption 2, we can decouple the complexity of $\mathcal{F}_{\mathcal{H}}$ using the complexity of \mathcal{H} via an analogous chain rule (Bartlett and Mendelson, 2002). Similar to (Tripuraneni et al, 2020), the loss ℓ_{net} obeys the following assumption.

Assumption 3. *The loss function ℓ_{net} satisfies $|\ell_{net}(\cdot, \cdot)| \leq B_l$ and $\ell_{net}(\cdot, \mathcal{X})$ is L_n -Lipschitz for all $\mathcal{X} \in \mathbb{X}$.*

For example, the mean squared error (MSE) $\frac{1}{M} \|\hat{\mathcal{X}} - \mathcal{X}\|^2$ is bounded by $4B_d^2$ and is $\frac{4B_d}{\sqrt{M}}$ -Lipschitz about the first input for all $\mathcal{X} \in \mathbb{X}$. Now, we present our main conclusion about the training error \mathbf{E}_{tr} .

Let $F^h := (f_1^h, \dots, f_T^h)$ denote the element in $\mathcal{F}_{\mathcal{H}}$. The empirical Rademacher complexity of $\mathcal{F}_{\mathcal{H}}$ is then defined as

$$\begin{aligned} \hat{\mathfrak{R}}_{\Sigma}(\mathcal{F}_{\mathcal{H}}) & := \mathbb{E}_{\Sigma} \left[\sup_{h \in \mathcal{H}} \frac{1}{T} \sum_{t=1}^T \frac{1}{N_t} \sum_{i_t=1}^{N_t} \sum_{m=1}^M \sigma_{ti_t m} f_t^h(\mathcal{Y}_{ti_t})_m \right], \\ & = \mathbb{E}_{\Sigma} \left[\sup_{h \in \mathcal{H}} \frac{1}{T} \sum_{t=1}^T \frac{1}{N_t} \sum_{i_t=1}^{N_t} \langle \sigma_{ti_t}, f_t^h(\mathcal{Y}_{ti_t}) \rangle \right], \end{aligned}$$

where $\Sigma = (\sigma_{11}, \dots, \sigma_{ti_t}, \dots, \sigma_{TN_T})$ and $\sigma_{ti_t} = (\sigma_{ti_t 1}, \dots, \sigma_{ti_t m})$, with $\sigma_{ti_t m}$ s following i.i.d uniform distribution on $\{-1, 1\}$. $(f_t^h)_m$ is the m -th element in f_t^h .

Theorem 1 (Training error). *Suppose that Assumptions 1, 2 and 3 hold. $\{R_t\}_{t=1}^T$ are convex and closed, and have subgradients. Then, for any*

$\delta > 0$, with probability at least $1 - \delta$, we have

$$\mathbf{E}_{tr} \leq 6L_n L_H \hat{\mathfrak{C}}_S(\mathcal{H}) + \frac{6B_l}{T} \sqrt{\sum_{t=1}^T \frac{1}{N_t}} \sqrt{\frac{\log \frac{2}{\delta}}{2}}.$$

Proof. The proof consists of several parts. We will firstly present an error bound (Mohri et al, 2018)(Shu et al, 2021) and then decouple the complexity of $\mathcal{F}_\mathcal{H}$ using Lemma 2.

1) Let $\mathcal{Q} := Q^{\otimes T}$ be a t -fold Cartesian product of function class Q , with element $\mathbf{q} = (q_1, \dots, q_T)$ and $q_t \in Q$ for all $t \in T$. The function q in Q satisfies $0 \leq q \leq B_l$. The data set $\mathbf{S} = \{z_{ti_t}\}_{i_t=1}^{N_t} \}_{t=1}^T$ consists of $\sum_t N_t$ data points i.i.d sampled from distribution D . For a $\mathbf{q} \in \mathcal{Q}$, let $\hat{\mathbb{E}}_{\mathbf{S}}[\mathbf{q}] = \frac{1}{T} \sum_{t=1}^T \frac{1}{N_t} \sum_{i_t=1}^{N_t} q_t(z_{ti_t})$, and $\mathbb{E}[\mathbf{q}] = \mathbb{E}[\hat{\mathbb{E}}_{\mathbf{S}}[\mathbf{q}]] = \frac{1}{T} \sum_{t=1}^T \mathbb{E}_{z \sim D}[q_t(z)]$.

We then define

$$\Phi(\mathbf{S}) = \sup_{\mathbf{q} \in \mathcal{Q}} \left(\mathbb{E}[\mathbf{q}] - \hat{\mathbb{E}}_{\mathbf{S}}[\mathbf{q}] \right).$$

Suppose that only one point z'_{ti_t} in \mathbf{S}' is different from z_{ti_t} in \mathbf{S} . Then

$$\begin{aligned} \Phi(\mathbf{S}') - \Phi(\mathbf{S}) &\leq \sup_{\mathbf{q} \in \mathcal{Q}} \left(\hat{\mathbb{E}}_{\mathbf{S}}[\mathbf{q}] - \hat{\mathbb{E}}_{\mathbf{S}'}[\mathbf{q}] \right), \\ &= \sup_{\mathbf{q} \in \mathcal{Q}} \left(\frac{q_t(z_{ti_t}) - q_t(z'_{ti_t})}{TN_t} \right) \leq \frac{B_l}{TN_t}. \end{aligned}$$

According to McDiarmid's inequality, we have

$$\begin{aligned} p[\Phi(\mathbf{S}) - \mathbb{E}_S[\Phi(\mathbf{S})] \geq \epsilon] &\leq \exp\left(\frac{T^2}{B^2} \frac{-2\epsilon^2}{\sum_{t=1}^T \frac{1}{N_t}}\right), \\ p[\Phi(\mathbf{S}) - \mathbb{E}_S[\Phi(\mathbf{S})] \leq -\epsilon] &\leq \exp\left(\frac{T^2}{B^2} \frac{-2\epsilon^2}{\sum_{t=1}^T \frac{1}{N_t}}\right). \end{aligned}$$

Let $\frac{\delta}{2} = \exp\left(\frac{T^2}{B^2} \frac{-2\epsilon^2}{\sum_{t=1}^T \frac{1}{N_t}}\right)$. Then, with probability at least $1 - \frac{\delta}{2}$, the following inequality holds:

$$\Phi(\mathbf{S}) \leq \mathbb{E}_S[\Phi(\mathbf{S})] + \frac{B}{T} \sqrt{\sum_{t=1}^T \frac{1}{N_t}} \sqrt{\frac{1}{2} \log \frac{\delta}{2}}.$$

Next, we estimate $\mathbb{E}_S[\Phi(\mathbf{S})]$ as follows:

$$\begin{aligned} \mathbb{E}_S[\Phi(\mathbf{S})] &= \mathbb{E}_S \left[\sup_{\mathbf{q} \in \mathcal{Q}} \left(\mathbb{E}[\mathbf{q}] - \hat{\mathbb{E}}_{\mathbf{S}}[\mathbf{q}] \right) \right] \\ &= \mathbb{E}_S \left[\sup_{\mathbf{q} \in \mathcal{Q}} \mathbb{E}_{\mathbf{S}'} \left[\hat{\mathbb{E}}_{\mathbf{S}'}[\mathbf{q}] - \hat{\mathbb{E}}_{\mathbf{S}}[\mathbf{q}] \right] \right] \\ &\leq \mathbb{E}_{\mathbf{S}, \mathbf{S}'} \left[\sup_{\mathbf{q} \in \mathcal{Q}} \left(\hat{\mathbb{E}}_{\mathbf{S}'}[\mathbf{q}] - \hat{\mathbb{E}}_{\mathbf{S}}[\mathbf{q}] \right) \right] \\ &= \mathbb{E}_{\mathbf{S}, \mathbf{S}'} \left[\sup_{\mathbf{q} \in \mathcal{Q}} \frac{1}{T} \sum_{t=1}^T \frac{1}{N_t} \sum_{i_t=1}^{N_t} (q_t(z'_{ti_t}) - q_t(z_{ti_t})) \right] \\ &= \mathbb{E}_{\Sigma, \mathbf{S}, \mathbf{S}'} \left[\sup_{\mathbf{q} \in \mathcal{Q}} \frac{1}{T} \sum_{t=1}^T \frac{1}{N_t} \sum_{i_t=1}^{N_t} \sigma_{ti_t} (q_t(z'_{ti_t}) - q_t(z_{ti_t})) \right] \\ &\leq \mathbb{E}_{\Sigma, \mathbf{S}'} \left[\sup_{\mathbf{q} \in \mathcal{Q}} \frac{1}{T} \sum_{t=1}^T \frac{1}{N_t} \sum_{i_t=1}^{N_t} \sigma_{ti_t} q_t(z'_{ti_t}) \right] + \\ &\quad \mathbb{E}_{\Sigma, \mathbf{S}} \left[\sup_{\mathbf{q} \in \mathcal{Q}} \frac{1}{T} \sum_{t=1}^T \frac{1}{N_t} \sum_{i_t=1}^{N_t} -\sigma_{ti_t} q_t(z_{ti_t}) \right] \\ &= 2\mathbb{E}_{\Sigma, \mathbf{S}} \left[\sup_{\mathbf{q} \in \mathcal{Q}} \frac{1}{T} \sum_{t=1}^T \frac{1}{N_t} \sum_{i_t=1}^{N_t} \sigma_{ti_t} q_t(z_{ti_t}) \right] \\ &= 2\mathfrak{R}(\mathcal{Q}). \end{aligned}$$

By using McDiarmid's inequality again to $\mathfrak{R}(\mathcal{Q})$, we have that with probability at least $1 - \frac{\delta}{2}$, the following inequality holds:

$$\mathfrak{R}(\mathcal{Q}) \leq \hat{\mathfrak{R}}_{\mathbf{S}}(\mathcal{Q}) + \frac{B}{T} \sqrt{\sum_{t=1}^T \frac{1}{N_t}} \sqrt{\frac{1}{2} \log \frac{\delta}{2}}.$$

Combining the above results, we have that with probability at least $1 - \delta$, the following inequality holds:

$$\mathbb{E}[\mathbf{q}] \leq \hat{\mathbb{E}}_{\mathbf{S}}[\mathbf{q}] + 2\hat{\mathfrak{R}}_{\mathbf{S}}(\mathcal{Q}) + 3\frac{B}{T} \sqrt{\sum_{t=1}^T \frac{1}{N_t}} \sqrt{\frac{1}{2} \log \frac{\delta}{2}}. \quad (\text{B12})$$

The first part of the proof is then completed. Just let $z_{ti_t} = (y_{ti_t}, x_{ti_t})$ and $q_t(z_{ti_t}) = \ell_{net}(f_t^h(y_{ti_t}, x_{ti_t}))$, we will get very close to the final training error estimation. But let us first decouple $\hat{\mathfrak{R}}_{\mathbf{S}}(\mathcal{Q})$ by some so-called contraction inequalities and Lemma 2, which leads to the second part of the proof.

2)

$$\begin{aligned}\hat{\mathfrak{R}}_{\mathbf{S}}(\mathcal{Q}) &= \mathbb{E}_{\Sigma} \left[\sup_{\mathcal{Q} \in \mathcal{Q}} \frac{1}{T} \sum_{t=1}^T \frac{1}{N_t} \sum_{i_t=1}^{N_t} \sigma_{ti_t} q_t(z_{ti_t}) \right] \\ &= \mathbb{E}_{\Sigma} \left[\sup_{h \in \mathcal{H}} \frac{1}{T} \sum_{t=1}^T \frac{1}{N_t} \sum_{i_t=1}^{N_t} \sigma_{ti_t} \ell_{net}(f_t^h(y_{ti_t}), x_{ti_t}) \right].\end{aligned}$$

According to (Maurer, 2016) and Assumption 3, we apply the vector-contraction inequality and get

$$\begin{aligned}\mathbb{E}_{\Sigma} \left[\sup_{h \in \mathcal{H}} \frac{1}{T} \sum_{t=1}^T \frac{1}{N_t} \sum_{i_t=1}^{N_t} \sigma_{ti_t} \ell_{net}(f_t^h(y_{ti_t}), x_{ti_t}) \right] &\leq \\ \sqrt{\frac{\pi}{2}} L_n \mathbb{E}_G \left[\sup_{h \in \mathcal{H}} \frac{1}{T} \sum_{t=1}^T \frac{1}{N_t} \sum_{i_t=1}^{N_t} \sum_{m=1}^M g_{ti_t m} f_t^h(y_{ti_t})_m \right],\end{aligned}$$

where $g_{ti_t m} \stackrel{i.i.d}{\sim} \mathcal{N}(0, 1)$, G is the set of all $g_{ti_t m}$ s and $f_t^h(y_{ti_t})_m$ is the m -th element of $f_t^h(y_{ti_t})$. The above inequality implies that

$$\hat{\mathfrak{R}}_{\mathbf{S}}(\mathcal{G}) \leq \sqrt{\frac{\pi}{2}} L_n \hat{\mathfrak{G}}_{\mathbf{S}}(\mathcal{F}_{\mathcal{H}}) \leq \frac{3}{2} L_n \hat{\mathfrak{G}}_{\mathbf{S}}(\mathcal{F}_{\mathcal{H}}).$$

We could further decouple $\hat{\mathfrak{G}}_{\mathbf{S}}(\mathcal{F}_{\mathcal{H}})$ using Lemma 2.

Similar to (Bartlett and Mendelson, 2002), we define two zero mean Gaussian processes

$$\begin{aligned}X_h &= \frac{1}{T} \sum_{t=1}^T \frac{1}{N_t} \sum_{i_t=1}^{N_t} \sum_{m=1}^M g_{ti_t m} f_t^h(y_{ti_t})_m, \\ Y_h &= \frac{1}{T} \sum_{t=1}^T \frac{1}{N_t} \sum_{i_t=1}^{N_t} \sum_{m=1}^M \bar{g}_{ti_t m} L_H h(y_{ti_t})_m.\end{aligned}$$

Then it can be deduced that:

$$\begin{aligned}\mathbb{E}_G [(X_h - X_{h'})^2] &= \mathbb{E}_G \left[\left[\frac{1}{T} \sum_{t=1}^T \frac{1}{N_t} \sum_{i_t=1}^{N_t} \sum_{m=1}^M (f_t^h(y_{ti_t})_m - f_t^{h'}(y_{ti_t})_m) g_{ti_t m} \right]^2 \right] \\ &= \frac{1}{T^2} \sum_{t=1}^T \frac{1}{N_t^2} \sum_{i_t=1}^{N_t} \sum_{m=1}^M \left(f_t^h(y_{ti_t})_m - f_t^{h'}(y_{ti_t})_m \right)^2\end{aligned}$$

$$\begin{aligned}&= \frac{1}{T^2} \sum_{t=1}^T \frac{1}{N_t^2} \sum_{i_t=1}^{N_t} \|f_t^h(y_{ti_t}) - f_t^{h'}(y_{ti_t})\|_2^2 \\ &\leq \frac{1}{T^2} \sum_{t=1}^T \frac{1}{N_t^2} \sum_{i_t=1}^{N_t} L_H^2 \|h(y_{ti_t}) - h'(y_{ti_t})\|_2^2 \\ &= \frac{1}{T^2} \sum_{t=1}^T \frac{1}{N_t^2} \sum_{i_t=1}^{N_t} \sum_{m=1}^M L_H^2 (h(y_{ti_t})_m - h'(y_{ti_t})_m)^2 \\ &= \mathbb{E}_{\bar{G}} \left[\left[\frac{1}{T} \sum_{t=1}^T \frac{1}{N_t} \sum_{i_t=1}^{N_t} \sum_{m=1}^M L_H (h(y_{ti_t})_m - h'(y_{ti_t})_m) \bar{g}_{ti_t m} \right]^2 \right] \\ &= \mathbb{E}_{\bar{G}} [(Y_h - Y_{h'})^2].\end{aligned}$$

The inequality above is derived by Lemma 2. Note that \mathcal{H} is a function class parameterized by a finite number of real-valued θ . Then applying the Sudakov-Fernique inequality to the general Gaussian process, we get

$$\mathbb{E}_G \left[\sup_{h \in \mathcal{H}} X_h \right] \leq \mathbb{E}_G \left[\sup_{h \in \mathcal{H}} Y_h \right],$$

which is equivalent to

$$\hat{\mathfrak{G}}_{\mathbf{S}}(\mathcal{F}_{\mathcal{H}}) \leq L_H \hat{\mathfrak{G}}_{\mathbf{S}}(\mathcal{H}).$$

The second part of the proof is then completed. Next, we will finally prove the proposed training error bound.

3)

$$\begin{aligned}\mathbf{E}_{tr} &= \mathbf{R}_{tr}(\hat{h}_{tr}) - \mathbf{R}_{tr}(h_{tr}^*) \\ &= \underbrace{\mathbf{R}_{tr}(\hat{h}_{tr}) - \hat{\mathbf{R}}_{tr}(\hat{h}_{tr})}_{(a)} + \underbrace{\hat{\mathbf{R}}_{tr}(\hat{h}_{tr}) - \hat{\mathbf{R}}_{tr}(h_{tr}^*)}_{(b)} \\ &\quad + \underbrace{\hat{\mathbf{R}}_{tr}(h_{tr}^*) - \mathbf{R}_{tr}(h_{tr}^*)}_{(c)}.\end{aligned}$$

According to the definition of \hat{h}_{tr} , (b) ≤ 0 . For (a)+(c), we directly estimate it by the result (B12) in the first part of this proof. With probability at least $1 - \delta$, the following inequality holds

$$(a) + (c) \leq 4\hat{\mathfrak{R}}_{\mathbf{S}}(\mathcal{Q}) + 6\frac{B}{T} \sqrt{\sum_{t=1}^T \frac{1}{N_t}} \sqrt{\frac{1}{2} \log \frac{\delta}{2}}$$

$$\begin{aligned} &\leq 6L_n \hat{\mathbf{G}}_{\mathbf{S}}(\mathcal{F}_{\mathcal{H}}) + 6\frac{B}{T} \sqrt{\sum_{t=1}^T \frac{1}{N_t} \sqrt{\frac{1}{2} \log \frac{\delta}{2}}} \\ &\leq 6L_n L_H \hat{\mathbf{G}}_{\mathbf{S}}(\mathcal{H}) + 6\frac{B}{T} \sqrt{\sum_{t=1}^T \frac{1}{N_t} \sqrt{\frac{1}{2} \log \frac{\delta}{2}}}. \end{aligned}$$

The whole proof is then completed. \square

B.3 Generalization Error Estimation

First, similar to the training error, we establish the test error for S target models defined in (9) as:

$$\mathbf{R}_{te}(h) := \frac{1}{S} \sum_{t=T+1}^{T+S} \mathbb{E}_{(\mathcal{Y}, \mathcal{X}) \sim \mathcal{D}} [\ell_{net}(f_{\lambda_t R_t}^h(\mathcal{Y}), \mathcal{X})],$$

where $\{R_t\}_{t=T+1}^{T+S}$ is usually different from $\{R_t\}_{t=1}^T$. The corresponding ‘‘best’’ HWnet for the new models can then be defined as:

$$h_0^* = \arg \min_{h \in \mathcal{H}} \mathbf{R}_{te}(h).$$

The generalization error is thus defined as:

$$\mathbf{E}_g := \mathbf{R}_{te}(\hat{h}_{tr}) - \mathbf{R}_{te}(h_0^*),$$

where $\mathbf{R}_{te}(\hat{h}_{tr})$ represents the test error on the trained HWnet \hat{h}_{tr} , and $\mathbf{R}_{te}(h_0^*)$ is the test error infimum on the hypothesis set \mathcal{H} . To estimate \mathbf{E}_g , our main challenge relies on measuring the divergence between the source and target models, i.e., calculating $\mathbf{R}_{te}(h) - \mathbf{R}_{tr}(h)$, because of the implicit form of $f_{\lambda R}^h$. We thus seek an approximation of $f_{\lambda R}^h$ to ease the calculation using the modified gradient step (Parikh and Boyd, 2014). Specifically, suppose R is differentiable, by taking the derivative of the objective function in Eq. (B7) concerning \mathcal{X} , the solution $\hat{\mathcal{X}}$ should satisfy:

$$\begin{aligned} &h^2 \odot (\hat{\mathcal{X}} - \mathcal{Y}) + \lambda \nabla R(\hat{\mathcal{X}}) = 0, \\ \Rightarrow \hat{\mathcal{X}} &= \left(\mathbf{I} + \frac{\lambda}{h^2} \odot \nabla R \right)^{-1}(\mathcal{Y}), \end{aligned} \quad (\text{B13})$$

where \mathbf{I} represents the identity mapping. The operator $(\mathbf{I} + g)^{-1}$ is known as the resolvent operator (Xie et al, 2022). If g is nonlinear, its

resolvent form is still implicit and difficult to analyze. Therefore, we approximate Eq. (B13) by using a linear transform to ∇R (Parikh and Boyd, 2014)(Xie et al, 2022):

$$\left(\mathbf{I} + \frac{\lambda}{h^2} \odot \nabla R \right)^{-1} \approx \mathbf{I} - \frac{\lambda}{h^2} \odot \nabla R. \quad (\text{B14})$$

The residual part of such approximation is $o(\lambda/h^2)$ as λ/h^2 goes to 0. In the rest of this section, we analyze the generalization error using the approximated form of $f_{\lambda R}^h$ as

$$\bar{f}_{\lambda R}^h := \mathbf{I} - \frac{\lambda}{h^2} \odot \nabla R. \quad (\text{B15})$$

It is easy to verify that $\bar{f}_{\lambda R}^h$ is \bar{L}_H -Lipschitz with respect to h . By utilizing Eq. (B15), we firstly present a lemma to estimate $|\mathbf{R}_{te}(h) - \mathbf{R}_{tr}(h)|$.

Lemma 3. *Suppose that the function $f_{\lambda R}^h$ takes the form of $\mathbf{I} - \frac{\lambda}{h^2} \odot \nabla R$ and ℓ_{net} is MSE loss. For any $h \in \mathcal{H}$, we have*

$$\begin{aligned} &|\mathbf{R}_{te}(h) - \mathbf{R}_{tr}(h)| \\ &\leq \mathbb{E}_{(\mathcal{Y}, \mathcal{X}) \sim \mathcal{D}} \left\{ \frac{4B_d}{\sqrt{M\varepsilon}} A_1 + \frac{1}{M\varepsilon^2} A_2 \right\}, \end{aligned}$$

where

$$A_1 = \left\| \left(\frac{1}{T} \sum_{t=1}^T \lambda_t \nabla R_t - \frac{1}{S} \sum_{t=T+1}^{T+S} \lambda_t \nabla R_t \right) (\mathcal{Y}) \right\|_2, \quad (\text{B16})$$

$$\begin{aligned} A_2 &= \left| \frac{1}{T} \sum_{t=1}^T \|(\lambda_t \nabla R_t) (\mathcal{Y})\|_2^2 - \right. \\ &\quad \left. \frac{1}{S} \sum_{t=T+1}^{T+S} \|(\lambda_t \nabla R_t) (\mathcal{Y})\|_2^2 \right|. \end{aligned} \quad (\text{B17})$$

Proof. For ease of notation, let $u_t^h = \frac{\lambda_t}{h} \odot \nabla R_t$.

$$\begin{aligned} &\mathbf{R}_{te}(h) - \mathbf{R}_{tr}(h) \\ &= \frac{1}{M} \mathbb{E}_{(\mathcal{Y}, \mathcal{X}) \sim \mathcal{D}} \left[\frac{1}{S} \sum_{t=T+1}^{T+S} \|\mathcal{Y} - u_t^h(\mathcal{Y}) - \mathcal{X}\|_2^2 - \right. \\ &\quad \left. \frac{1}{T} \sum_{t=1}^T \|\mathcal{Y} - u_t^h(\mathcal{Y}) - \mathcal{X}\|_2^2 \right] \end{aligned}$$

$$\begin{aligned}
&= \frac{1}{M} \mathbb{E}_{\mathcal{D}} \left[\frac{1}{S} \sum_{t=T+1}^{T+S} \|u_t^h(\mathcal{Y})\|_2^2 - \frac{1}{T} \sum_{t=1}^T \|u_t^h(\mathcal{Y})\|_2^2 \right. \\
&\quad \left. + 2 \left\langle \mathcal{Y} - \mathcal{X}, \frac{1}{T} \sum_{t=1}^T u_t^h(\mathcal{Y}) - \frac{1}{S} \sum_{t=T+1}^{T+S} u_t^h(\mathcal{Y}) \right\rangle \right] \\
&\Rightarrow |\mathbf{R}_{te}(h) - \mathbf{R}_{tr}(h)| \\
&\leq \frac{1}{M} \mathbb{E}_{\mathcal{D}} \left[\left| \frac{1}{S} \sum_{t=T+1}^{T+S} \|u_t^h(\mathcal{Y})\|_2^2 - \frac{1}{T} \sum_{t=1}^T \|u_t^h(\mathcal{Y})\|_2^2 \right| \right. \\
&\quad \left. + 2 \|\mathcal{Y} - \mathcal{X}\|_2 \left\| \frac{1}{T} \sum_{t=1}^T u_t^h(\mathcal{Y}) - \frac{1}{S} \sum_{t=T+1}^{T+S} u_t^h(\mathcal{Y}) \right\|_2 \right].
\end{aligned}$$

Note that

$$\begin{aligned}
&\left| \frac{1}{S} \sum_{t=T+1}^{T+S} \|u_t^h(\mathcal{Y})\|_2^2 - \frac{1}{T} \sum_{t=1}^T \|u_t^h(\mathcal{Y})\|_2^2 \right| \\
&\leq \frac{1}{\varepsilon^2} \left| \frac{1}{S} \sum_{t=T+1}^{T+S} \|\lambda_t \nabla R_t(\mathcal{Y})\|_2^2 - \frac{1}{T} \sum_{t=1}^T \|\lambda_t \nabla R_t(\mathcal{Y})\|_2^2 \right| \\
&:= \frac{1}{\varepsilon^2} A_2
\end{aligned}$$

and

$$\begin{aligned}
&\|\mathcal{Y} - \mathcal{X}\|_2 \left\| \frac{1}{T} \sum_{t=1}^T u_t^h(\mathcal{Y}) - \frac{1}{S} \sum_{t=T+1}^{T+S} u_t^h(\mathcal{Y}) \right\|_2 \\
&\leq \frac{2B_d \sqrt{M}}{\varepsilon} \left\| \frac{1}{T} \sum_{t=1}^T \lambda_t \nabla R_t(\mathcal{Y}) - \frac{1}{S} \sum_{t=T+1}^{T+S} \lambda_t \nabla R_t(\mathcal{Y}) \right\|_2 \\
&:= \frac{2B_d \sqrt{M}}{\varepsilon} A_1.
\end{aligned}$$

Then we have

$$\begin{aligned}
|\mathbf{R}_{te}(h) - \mathbf{R}_{tr}(h)| &\leq \frac{1}{M} \mathbb{E}_{\mathcal{D}} \left[\frac{4B_d \sqrt{M}}{\varepsilon} A_1 + \frac{1}{\varepsilon^2} A_2 \right] \\
&= \mathbb{E}_{(\mathcal{Y}, \mathcal{X}) \sim \mathcal{D}} \left[\frac{4B_d}{\sqrt{M} \varepsilon} A_1 + \frac{1}{M \varepsilon^2} A_2 \right].
\end{aligned}$$

The proof is then completed. \square

Based on Lemma 3, we can directly estimate the generalization error \mathbf{E}_g as follows.

Theorem 2 (Generalization error). *Suppose that Assumptions 1, 2 and 3 hold, $\{R_t\}_{t=0}^T$ are convex and closed, $\tilde{f}_{\lambda R}^h$ takes the form of $\mathbf{I} - \frac{\lambda}{h^2} \odot$*

∇R , and ℓ_{net} is MSE loss. Then for any $\delta > 0$, with probability at least $1 - \delta$, we have

$$\begin{aligned}
\mathbf{E}_g &\leq 6L_n \bar{L}_H \hat{\Theta}_S(\mathcal{H}) + \frac{6B_l}{T} \sqrt{\sum_{t=1}^T \frac{1}{N_t}} \sqrt{\frac{\log \frac{2}{\delta}}{2}} \\
&\quad + \mathbb{E}_{(\mathcal{Y}, \mathcal{X}) \sim \mathcal{D}} \left\{ \frac{8B_d}{\sqrt{M} \varepsilon} A_1 \right\} + \mathbb{E}_{(\mathcal{Y}, \mathcal{X}) \sim \mathcal{D}} \left\{ \frac{2}{M \varepsilon^2} A_2 \right\},
\end{aligned}$$

where A_1 takes the form of (B16) and A_2 of (B17).

Proof.

$$\begin{aligned}
\mathbf{E}_g &= \mathcal{R}_{te}(\hat{h}_{tr}) - \mathcal{R}_{te}(h_0^*) \\
&= \underbrace{\mathcal{R}_{te}(\hat{h}_{tr}) - \mathcal{R}_{tr}(\hat{h}_{tr})}_{(a)} + \underbrace{\mathcal{R}_{tr}(\hat{h}_{tr}) - \mathcal{R}_{tr}(h_{tr}^*)}_{(b)} + \\
&\quad \underbrace{\mathcal{R}_{tr}(h_{tr}^*) - \mathcal{R}_{tr}(h_0^*)}_{(c)} + \underbrace{\mathcal{R}_{tr}(h_0^*) - \mathcal{R}_{te}(h_0^*)}_{(d)}.
\end{aligned}$$

According to the definition of h_{tr}^* , we get (c) ≤ 0 . (b) is the training error that we have estimated as in Theorem 1. And by Lemma 3, we can directly get

$$(a) + (c) \leq \mathbb{E}_{(\mathcal{Y}, \mathcal{X}) \sim \mathcal{D}} \left[\frac{8B_d}{\sqrt{M} \varepsilon} A_1 + \frac{2}{M \varepsilon^2} A_2 \right].$$

Then, the final result is achieved. \square

References

- Aggarwal HK, Majumdar A (2016) Hyperspectral image denoising using spatio-spectral total variation. *IEEE Geoscience and Remote Sensing Letters* 13(3):442–446
- Arad B, Ben-Shahar O (2016) Sparse recovery of hyperspectral signal from natural rgb images. In: *European Conference on Computer Vision*, Springer, pp 19–34
- Bartlett PL, Mendelson S (2002) Rademacher and gaussian complexities: Risk bounds and structural results. *Journal of Machine Learning Research* 3(Nov):463–482
- Beck A (2017) *First-Order Methods in Optimization*. Society for Industrial and Applied Mathematics

- Ben-David S, Blitzer J, Crammer K, et al (2010) A theory of learning from different domains. *Machine Learning* 79(1):151–175
- Blanchard G, Lee G, Scott C (2011) Generalizing from several related classification tasks to a new unlabeled sample. *Advances in Neural Information Processing Systems* 24
- Blanchard G, Deshmukh AA, Dogan Ü, et al (2021) Domain generalization by marginal transfer learning. *The Journal of Machine Learning Research* 22(1):46–100
- Bodrito T, Zouaoui A, Chanussot J, et al (2021) A trainable spectral-spatial sparse coding model for hyperspectral image restoration. *Advances in Neural Information Processing Systems* 34:5430–5442
- Boyd S, Parikh N, Chu E, et al (2011) Distributed optimization and statistical learning via the alternating direction method of multipliers. *Foundations and Trends® in Machine Learning* 3(1):1–122
- Candes EJ, Wakin MB, Boyd SP (2008) Enhancing sparsity by reweighted ℓ_1 minimization. *Journal of Fourier Analysis and Applications* 14(5):877–905
- Cao X, Zhao Q, Meng D, et al (2016) Robust low-rank matrix factorization under general mixture noise distributions. *IEEE Transactions on Image Processing* 25(10):4677–4690
- Cao X, Fu X, Xu C, et al (2021) Deep spatial-spectral global reasoning network for hyperspectral image denoising. *IEEE Transactions on Geoscience and Remote Sensing* 60:1–14
- Chang Y, Yan L, Zhong S (2017) Hyperlaplacian regularized unidirectional low-rank tensor recovery for multispectral image denoising. In: *Proceedings of the IEEE Conference on Computer Vision and Pattern Recognition*, pp 4260–4268
- Chang Y, Yan L, Fang H, et al (2018) Hsi-denet: Hyperspectral image restoration via convolutional neural network. *IEEE Transactions on Geoscience and Remote Sensing* 57(2):667–682
- Chen Y, Cao X, Zhao Q, et al (2017a) Denoising hyperspectral image with non-iid noise structure. *IEEE Transactions on Cybernetics* 48(3):1054–1066
- Chen Y, Guo Y, Wang Y, et al (2017b) Denoising of hyperspectral images using nonconvex low rank matrix approximation. *IEEE Transactions on Geoscience and Remote Sensing* 55(9):5366–5380
- Chen Y, He W, Yokoya N, et al (2019) Nonlocal tensor-ring decomposition for hyperspectral image denoising. *IEEE Transactions on Geoscience and Remote Sensing* 58(2):1348–1362
- Cortes C, Mohri M (2011) Domain adaptation in regression. In: *International Conference on Algorithmic Learning Theory*, Springer, pp 308–323
- Dai Wenyuan YQ, Guirong X, Yong Y (2007) Boosting for transfer learning. In: *International Conference on Machine Learning*, pp 193–200
- Germain P, Habrard A, Laviolette F, et al (2016) A new pac-bayesian perspective on domain adaptation. In: *International Conference on Machine Learning*, PMLR, pp 859–868
- Gu S, Xie Q, Meng D, et al (2017) Weighted nuclear norm minimization and its applications to low level vision. *International Journal of Computer Vision* 121(2):183–208
- He W, Zhang H, Zhang L, et al (2015a) Hyperspectral image denoising via noise-adjusted iterative low-rank matrix approximation. *IEEE Journal of Selected Topics in Applied Earth Observations and Remote Sensing* 8(6):3050–3061
- He W, Zhang H, Zhang L, et al (2015b) Total-variation-regularized low-rank matrix factorization for hyperspectral image restoration. *IEEE Transactions on Geoscience and Remote Sensing* 54(1):178–188
- He W, Yao Q, Li C, et al (2020) Non-local meets global: An integrated paradigm for hyperspectral image restoration. *IEEE Transactions on Pattern Analysis and Machine Intelligence*

- Jiang C, Zhang H, Zhang L, et al (2016) Hyperspectral image denoising with a combined spatial and spectral weighted hyperspectral total variation model. *Canadian Journal of Remote Sensing* 42(1):53–72
- Jiang TX, Zhuang L, Huang TZ, et al (2021) Adaptive hyperspectral mixed noise removal. *IEEE Transactions on Geoscience and Remote Sensing* 60:1–13
- Kalman LS, Bassett III EM (1997) Classification and material identification in an urban environment using hydice hyperspectral data. In: *Imaging Spectrometry III*, SPIE, pp 57–68
- Kingma DP, Ba J (2014) Adam: A method for stochastic optimization. *arXiv preprint arXiv:1412.6980*
- Lehtinen J, Munkberg J, Hasselgren J, et al (2018) Noise2noise: Learning image restoration without clean data. In: *International Conference on Machine Learning*, PMLR, pp 2965–2974
- Li M, Fu Y, Zhang Y (2023a) Spatial-spectral transformer for hyperspectral image denoising. In: *Proceedings of the AAAI Conference on Artificial Intelligence*, pp 1368–1376
- Li M, Liu J, Fu Y, et al (2023b) Spectral enhanced rectangle transformer for hyperspectral image denoising. In: *Proceedings of the IEEE/CVF Conference on Computer Vision and Pattern Recognition*, pp 5805–5814
- Lin B, Tao X, Lu J (2019) Hyperspectral image denoising via matrix factorization and deep prior regularization. *IEEE Transactions on Image Processing* 29:565–578
- Lin J, Huang TZ, Zhao XL, et al (2020) A tensor subspace representation-based method for hyperspectral image denoising. *IEEE Transactions on Geoscience and Remote Sensing* 59(9):7739–7757
- Liu D, Sun DW, Zeng XA (2014) Recent advances in wavelength selection techniques for hyperspectral image processing in the food industry. *Food and Bioprocess Technology* 7(2):307–323
- Lu B, Dao PD, Liu J, et al (2020) Recent advances of hyperspectral imaging technology and applications in agriculture. *Remote Sensing* 12(16):2659
- Lu T, Li S, Fang L, et al (2015) Spectral-spatial adaptive sparse representation for hyperspectral image denoising. *IEEE Transactions on Geoscience and Remote Sensing* 54(1):373–385
- Luo YS, Zhao XL, Jiang TX, et al (2021) Hyperspectral mixed noise removal via spatial-spectral constrained unsupervised deep image prior. *IEEE Journal of Selected Topics in Applied Earth Observations and Remote Sensing* 14:9435–9449
- Ma Y, Li C, Mei X, et al (2016) Robust sparse hyperspectral unmixing with $\ell_{2,1}$ norm. *IEEE Transactions on Geoscience and Remote Sensing* 55(3):1227–1239
- Mahmud M, Ray S (2007) Transfer learning using kolmogorov complexity: Basic theory and empirical evaluations. *Advances in Neural Information Processing Systems* 20
- Manolakis DG, Lockwood RB, Cooley TW (2016) *Hyperspectral imaging remote sensing: physics, sensors, and algorithms*. Cambridge University Press
- Maurer A (2016) A vector-contraction inequality for rademacher complexities. In: *International Conference on Algorithmic Learning Theory*, Springer, pp 3–17
- Maurer A, Pontil M, Romera-Paredes B (2016) The benefit of multitask representation learning. *Journal of Machine Learning Research* 17(81):1–32
- McNamara D, Balcan MF (2017) Risk bounds for transferring representations with and without fine-tuning. In: *International Conference on Machine Learning*, PMLR, pp 2373–2381
- Meng D, De La Torre F (2013) Robust matrix factorization with unknown noise. In: *Proceedings of the IEEE International Conference on Computer Vision*, pp 1337–1344

- Mohri M, Rostamizadeh A, Talwalkar A (2018) Foundations of machine learning. MIT press
- Muandet K, Balduzzi D, Schölkopf B (2013) Domain generalization via invariant feature representation. In: International Conference on Machine Learning, PMLR, pp 10–18
- Pang L, Gu W, Cao X (2022) Trq3dnet: A 3d quasi-recurrent and transformer based network for hyperspectral image denoising. Remote Sensing 14(18)
- Parikh N, Boyd S (2014) Proximal algorithms. Foundations and Trends® in Optimization 1(3):127–239
- Peng J, Xie Q, Zhao Q, et al (2020) Enhanced 3d tv regularization and its applications on hsi denoising and compressed sensing. IEEE Transactions on Image Processing 29:7889–7903
- Peng J, Wang H, Cao X, et al (2022a) Fast noise removal in hyperspectral images via representative coefficient total variation. IEEE Transactions on Geoscience and Remote Sensing 60:1–17
- Peng J, Wang Y, Zhang H, et al (2022b) Exact decomposition of joint low rankness and local smoothness plus sparse matrices. IEEE Transactions on Pattern Analysis and Machine Intelligence pp 1–16
- Pyo J, Duan H, Baek S, et al (2019) A convolutional neural network regression for quantifying cyanobacteria using hyperspectral imagery. Remote Sensing of Environment 233:111350
- Qiu Z, Yao T, Mei T (2017) Learning spatio-temporal representation with pseudo-3d residual networks. In: Proceedings of the IEEE International Conference on Computer Vision, pp 5533–5541
- Rasti B, Ulfarsson MO, Ghamisi P (2017) Automatic hyperspectral image restoration using sparse and low-rank modeling. IEEE Geoscience and Remote Sensing Letters 14(12):2335–2339
- Rui X, Cao X, Xie Q, et al (2021) Learning an explicit weighting scheme for adapting complex hsi noise. In: Proceedings of the IEEE Conference on Computer Vision and Pattern Recognition, pp 6739–6748
- Shi Q, Tang X, Yang T, et al (2021) Hyperspectral image denoising using a 3-d attention denoising network. IEEE Transactions on Geoscience and Remote Sensing 59(12):10348–10363
- Shi W, Ling Q, Wu G, et al (2015) A proximal gradient algorithm for decentralized composite optimization. IEEE Transactions on Signal Processing 63(22):6013–6023
- Shu J, Meng D, Xu Z (2021) Learning an explicit hyperparameter prediction policy conditioned on tasks. arXiv preprint arXiv:210702378
- Sicilia A, Zhao X, Hwang SJ (2021) Domain adversarial neural networks for domain generalization: When it works and how to improve. arXiv preprint arXiv:210203924
- Sun Y, Yang Y, Liu Q, et al (2020) Learning non-locally regularized compressed sensing network with half-quadratic splitting. IEEE Transactions on Multimedia 22(12):3236–3248
- Tripuraneni N, Jordan M, Jin C (2020) On the theory of transfer learning: The importance of task diversity. Advances in Neural Information Processing Systems 33:7852–7862
- Ulyanov D, Vedaldi A, Lempitsky V (2018) Deep image prior. In: Proceedings of the IEEE Conference on Computer Vision and Pattern Recognition, pp 9446–9454
- Wang P (2019) Image denoising using deep cgan with bi-skip connections. In: Proceedings of the IEEE/CVF Conference on Computer Vision and Pattern Recognition Workshops, pp 0–0
- Wang Y, Peng J, Zhao Q, et al (2017) Hyperspectral image restoration via total variation regularized low-rank tensor decomposition. IEEE Journal of Selected Topics in Applied Earth Observations and Remote Sensing 11(4):1227–1243

- Wei K, Fu Y, Huang H (2020) 3-d quasi-recurrent neural network for hyperspectral image denoising. *IEEE Transactions on Neural Networks and Learning Systems* 32(1):363–375
- Wei W, Zhang L, Tian C, et al (2017) Structured sparse coding-based hyperspectral imagery denoising with intracluster filtering. *IEEE Transactions on Geoscience and Remote Sensing* 55(12):6860–6876
- Xie Q, Zhao Q, Meng D, et al (2017) Kronecker-basis-representation based tensor sparsity and its applications to tensor recovery. *IEEE Transactions on Pattern Analysis and Machine Intelligence* 40(8):1888–1902
- Xie X, Wang Q, Ling Z, et al (2022) Optimization induced equilibrium networks: An explicit optimization perspective for understanding equilibrium models. *IEEE Transactions on Pattern Analysis and Machine Intelligence* pp 1–14
- Xiong F, Tao S, Zhou J, et al (2020) Smds-net: Model guided spectral-spatial network for hyperspectral image denoising. *arXiv preprint arXiv:201201829*
- Xiong F, Zhou J, Zhao Q, et al (2021) Mac-net: Model-aided nonlocal neural network for hyperspectral image denoising. *IEEE Transactions on Geoscience and Remote Sensing* 60:1–14
- Xue J, Zhao Y, Liao W, et al (2019) Nonlocal low-rank regularized tensor decomposition for hyperspectral image denoising. *IEEE Transactions on Geoscience and Remote Sensing* 57(7):5174–5189
- Yasuma F, Mitsunaga T, Iso D, et al (2010) Generalized assorted pixel camera: postcapture control of resolution, dynamic range, and spectrum. *IEEE transactions on image processing* 19(9):2241–2253
- Yuan Q, Zhang L, Shen H (2012) Hyperspectral image denoising employing a spectral-spatial adaptive total variation model. *IEEE Transactions on Geoscience and Remote Sensing* 50(10):3660–3677
- Yuan Q, Zhang Q, Li J, et al (2018) Hyperspectral image denoising employing a spatial-spectral deep residual convolutional neural network. *IEEE Transactions on Geoscience and Remote Sensing* 57(2):1205–1218
- Yue Z, Meng D, Sun Y, et al (2018) Hyperspectral image restoration under complex multi-band noises. *Remote Sensing* 10(10):1631
- Zhang H, He W, Zhang L, et al (2013) Hyperspectral image restoration using low-rank matrix recovery. *IEEE Transactions on Geoscience and Remote Sensing* 52(8):4729–4743
- Zhang H, Liu L, He W, et al (2019) Hyperspectral image denoising with total variation regularization and nonlocal low-rank tensor decomposition. *IEEE Transactions on Geoscience and Remote Sensing* 58(5):3071–3084
- Zhang T, Fu Y, Li C (2021) Hyperspectral image denoising with realistic data. In: *Proceedings of the IEEE/CVF International Conference on Computer Vision*, pp 2248–2257
- Zhang T, Fu Y, Zhang J (2022) Guided hyperspectral image denoising with realistic data. *International Journal of Computer Vision* 130(11):2885–2901
- Zhao YQ, Yang J (2014) Hyperspectral image denoising via sparse representation and low-rank constraint. *IEEE Transactions on Geoscience and Remote Sensing* 53(1):296–308
- Zheng YB, Huang TZ, Zhao XL, et al (2020) Double-factor-regularized low-rank tensor factorization for mixed noise removal in hyperspectral image. *IEEE Transactions on Geoscience and Remote Sensing* 58(12):8450–8464
- Zhuang L, Ng MK (2021) Fasthymix: Fast and parameter-free hyperspectral image mixed noise removal. *IEEE Transactions on Neural Networks and Learning Systems* pp 1–15
- Zhuang L, Ng MK, Gao L, et al (2023) Eigenimage2eigenimage (e2e): A self-supervised deep learning network for hyperspectral image denoising. *IEEE Transactions on Neural Networks and Learning Systems*